

Concentric Dual Throat Aerospike and De Laval Rocket Nozzle with Dual Expander Cycle

A project presented to
the Faculty of the Department of Aerospace Engineering at San Jose State University

In partial fulfillment of the requirements for the degree
Master of Science in Aerospace Engineering

by
Jordan M.D. Pollard
May 2022

Approved by

Dr Periklis E. Papadopoulos
Faculty Advisor



© 2022

Jordan Pollard

ALL RIGHTS RESERVED

Abstract

This document details a systems-level research and development project regarding the integration of a conventional de-Laval rocket nozzle into the base truncation of a toroidal aerospike. This was done with the intent of introducing a nozzle design for the purpose of martian sample return missions. This unconventional configuration of a concentric, alternate expansion mode, fixed geometry, and dual throat nozzle will be referred to as a 'compound nozzle' throughout the duration of the study. In addition to the novel nozzle configuration, a liquid oxygen and liquid hydrogen dual expander cycle is detailed and intended for integration with the nozzle, taking advantage of the extreme heat generated through the novel nozzle design. The initial mission profile and nozzle geometry is calculated through the use of Matlab calculations and supplementing software. The performance of the engine is further investigated through the use of the computational fluid dynamics software ANSYS fluent. Ultimately while the final design iteration of the compound nozzle does perform as expected with respect to the inner and outer flow regimes, the performance improvements are low compared to a similar-sized system of either constituent configuration. With the final performance of roughly 412s and 394s specific impulse for the outer and inner nozzle respectively. Consequently, further development of the concept is required to attain greater performance improvements over more conventional systems.

I. Contents

I.	Contents	iv
II.	Figures	vi
III.	Tables	vii
IV.	Nomenclature	viii
1.	Introduction	1
1.1	Project motivation	1
1.2	Project objective	1
1.3	Literature review	2
1.3.1	De Laval rocket nozzles	3
1.3.2	Aerospike rocket nozzles	4
1.3.3	Dual Throat nozzles	7
1.3.4	Combustion cycles	7
1.4	Methodology	9
2.	Intended System Purpose	10
2.1	Nozzle application	10
2.2	Mission profile	10
3.	Nozzle system design	15
3.1	Nozzle profile	15
3.2	Annular nozzle design	15
3.3	De Laval nozzle design	19
3.4	Dual throat configuration	21
4.	Combustion cycle design	24
4.1	Combustion cycle profile	24
4.2	Combustion cycle architecture	25
4.3	Combustion cycle integration	27
5.	Coolant system design	28
5.1	Coolant system profile	28
5.2	Coolant system decomposition	28
5.3	Coolant system architecture	29
6.	Computational fluid dynamics analysis	33
6.1	Single throat operation	39
6.1.1	De Laval throat operation	39
6.1.2	Annular throat operation	41
6.2	Dual throat operation	42
6.3	Altitude study	44
7.	Discussion	47

8.	Future Development.....	48
9.	Conclusions	49
	Acknowledgments.....	50
	References	51
	Appendix A- Simple Ideal Rocket Theory Calculation Code.....	53
	Appendix B- Orbit Transfer Trajectory Code.....	55
	Appendix C- Inner Nozzle Contour.....	60
	Appendix D- Aerospike Contour.....	63

II. Figures

Figure. 1.1:	Contemporary rocket nozzle configuration	3
Figure. 1.2:	Expansion properties of a De Laval nozzle	4
Figure. 1.3:	Toroidal aerospike nozzle configuration	4
Figure. 1.4:	Exhaust flow/expansion characteristics of aerospike nozzle	5
Figure. 1.5:	Anatomy of truncated aerospike nozzle flow.	6
Figure. 1.6:	Dual throat nozzle flow at sea level and high-altitude operation	7
Figure. 1.7:	Gas generator cycle	8
Figure. 1.8:	Diagram of a staged combustion cycle	9
Figure. 1.9:	Velocity contour of outer nozzle operational mode 50,000 Pa.....	45
Chapter 2		
Figure. 2.1:	Visualization of theoretical mission profile	11
Figure. 2.2:	Earth to mars Hohman transfer	13
Chapter 3.....		
Figure. 3.1:	Aerospike nozzle contour dimensions	16
Figure. 3.2:	Cowl to center body relation variables	17
Figure. 3.3:	Aerospike center body contour.....	18
Figure. 3.4:	Illustration of the method of characteristics	19
Figure. 3.5:	Convergent divergent nozzle contour	21
Figure. 3.6:	Illustration of initial compound nozzle iterations	22
Figure. 3.7:	Final compound nozzle configuration	23
Chapter 4.....		
Figure. 4.1:	Closed expander cycle	25
Figure. 4.2:	Simple P&ID of dual expander cycle	27
Chapter 5		
Figure. 5.1:	Regenerative cooling channel profile	28
Figure. 5.2:	Regenerative cooling heat transfer profile.....	29
Figure. 5.3:	Visual representation of Regenerative cooling channels in the center nozzle..	30
Figure. 5.4:	Integration of regenerative cooling channels into the compound nozzle	31
Figure. 5.5:	Inner nozzle temperature relative to the position.....	32
Figure. 5.6:	Inner nozzle total heat flux relative to the position.....	32
Chapter 6		
Figure. 6.1:	Simplified nozzle geometry for CFD import initial configuration	33
Figure. 6.2:	Simplified nozzle geometry for CFD import Final configuration	34
Figure. 6.3:	View of fluent meshing topology initial configuration.....	34
Figure. 6.4:	View of fluent meshing topology final configuration.....	35
Figure. 6.5:	Mach contour of center nozzle operational mode (initial design)	40
Figure. 6.6:	Mach contour of center nozzle operational mode (final design)	40
Figure. 6.7:	Mach contour of annular nozzle operational mode.....	41
Figure. 6.8:	Alternate initial nozzle geometry simulation.....	41
Figure. 6.9:	Final nozzle configuration simulation (aerospike)	42
Figure. 6.10:	Mach contour of dual nozzle Operational mode.....	43
Figure. 6.11:	Final compound nozzle configuration run (dual throat)	43
Figure. 6.12:	Mach contour of dual nozzle operational mode 50,000 Pa.....	44
Figure. 6.13:	Velocity contour of dual nozzle operational mode 50,000 Pa	45
Figure. 6.14:	3D nozzle flow representation (dual mode).....	46

III. Tables

Table 2.1:	Centaur III specifications.....	12
Table 2.2:	Mission profile constants	14
Chapter 3.....		
Table 3.1:	Derived values for aerospike	18
Table 3.2:	Aerospike center body contour	18
Table 3.3:	Thrust and mass flow rates of inner nozzle	21
Chapter 6.....		
Table 6.1:	Compound Nozzle designs: General Settings.....	35
Table 6.2:	Compound nozzle designs 1-2: boundary conditions	36
Table 6.3:	Compound nozzle Final Design: boundary conditions.....	37
Table 6.4:	Compound nozzle: solution methods.....	38
Table 6.5:	Compound nozzle designs 1-2: solution initialization.....	39

IV. Nomenclature

A_e	=	Area of nozzle exit	P_e	=	Nozzle exit pressure
CFD	=	Computational fluid dynamics	R	=	ideal gas constant
G_0	=	Gravitational constant	R_1	=	Radius of Aerospike ramp peak
gr_T	=	Truncation height	r_{1c}	=	Convergent angle 1
I_{sp}	=	Specific Impulse	R_2	=	Inner radius of cowl lip
L_{cn}	=	Length of convergent nozzle	r_{AR}	=	External cowl height
L_{ns}	=	Length of nozzle spike	R_{AZ}	=	Lower height of cowl
\dot{m}	=	mass flow rate	r_x	=	Ramp iteration height
M_o	=	Initial mass	T_c	=	Chamber temperature
M_p	=	Propellant mass	V	=	velocity
M_{pl}	=	Payload mass	V_e	=	Nozzle exit velocity
MR	=	Vehicle mass ratio	V_{eq}	=	Equivalent velocity
M_w	=	Molecular weight	α	=	Internal cowl angle
P_a	=	Ambient pressure	β	=	Convergent nozzle angle
P_c	=	Chamber pressure	γ	=	Ratio of specific heats
Δv	=	Change in velocity	$P\&ID$	=	Plumbing and Instrumentation Diagram
ε	=	A/At expansion ratio	MFV	=	Main fuel Valve
θ_t	=	thrust angle	MOV	=	Main Oxidizer Valve
F	=	thrust	SV	=	Shutoff Valve

1. Introduction

The following document describes a systems-level investigation into the integration of a traditional convergent-divergent expansion nozzle into the base truncation of an altitude compensating aerospike nozzle with a toroidal configuration. The integration of these independent systems into a dual throat nozzle consists of two parallel design approaches. The initial design approach consists of a top-level systems design for the nozzle and accompanying combustion cycle. The second design approach running in parallel is the utilization of computational fluid dynamics to perform a foundational analysis and characterization of the nozzle design performance and exhaust flow characteristics at varying altitudes. The newly integrated dual nozzle system will be referred to as the “Compound nozzle” and will incorporate a dual expander cycle utilizing liquid hydrogen for fuel and liquid oxygen for oxidizer. This innovative design could represent a significant improvement over conventional nozzle design. With control over the center body flow allowing for control over the ambient conditions of the exit at the convergent-divergent nozzle and compensating its negative expansion properties while simultaneously providing greater thrust to the nozzle at higher pressure conditions. The details of the associated system components will be described in the subsequent chapters.

1.1 Project motivation

Since the development of large-scale rocket engines, conventional nozzle design has been nearly ubiquitous in almost all design efforts. This is problematic due to the fact that most conventional convergent-divergent rocket nozzle designs suffer from significant inefficiencies that can only be compensated through the use of complex and heavy variable geometries or multiple engine design variants for the various stages of operation. Further compounding the issue, is the use of fixed geometry nozzles that cannot compensate for alterations in expansion conditions. This not only drives up the cost and complexity of individual launch platforms which not only require multiple boosters and stages as a result but significantly limits exploration into alternative means of propulsion. The nozzle design proposed here stands to greatly improve upon the performance and versatility of traditional engine systems while compensating for the shortcomings of both of the constituent integrated systems.

1.2 Project objective

The objective of this investigation is the coupling of a convergent-divergent nozzle and a truncated toroidal aerospike nozzle into a dual throat nozzle. The coupling of these systems should allow for compensation for the weaknesses in each respective design. Consequently, this project consists of three main sections. The first portion will concern the basic design of the nozzle and a systems-level design of the associated subsystems of the new engine. The second section details the computational analysis of the novel design and the subsequent performance metrics and flow characteristics observed. The last will be the detailing of a potential mission profile for such as system. The unconventional configuration of a concentric, alternate expansion mode, fixed geometry, and dual throat nozzle will be referred to as a ‘compound nozzle’ though the duration of this paper. The aforementioned system design, intended mission profile, and performance analysis will be detailed in the subsequent chapters.

1.3 Literature review

The basic concept of a rocket is predicated on Newton's Third Law of motion, which states that for every action there is an equal and opposite reaction. More specifically, the expulsion of high-speed gasses exerts an equivalent force upon the rocket in the opposite direction, thereby generating thrust. Most modern large-scale rockets utilize a type of rocket engine known as a liquid propellant engine. These rocket engines take advantage of the aforementioned principle through the high-pressure combustion of chemical propellants. Most commonly these propellants are separated into two components, a fuel, and an oxidizer. These propellants are often pumped under pressure from tanks into the rocket combustion chamber and ignited. This process allows for the generation of extreme temperatures and pressures in the reaction product gasses which subsequently are accelerated through a supersonic nozzle and ejected at extremely high velocity, thereby imparting momentum to the vehicle.

The nozzle portion of a rocket engine thrust chamber inhabits an extremely vital role in the functionality of the engine, as the nozzle design dictates the engine's performance characteristics throughout the duration of the engine operation. The most common nozzle configuration consists of a converging section, a constriction or throat, and a diverging section. The diverging section of the nozzle is often either a simple conical section or a parabolic bell shape. A simplified illustration of such a rocket engine is depicted in figure 1 below.

In addition to the conventional convergent-divergent nozzle design configurations, there are more unconventional designs that have unique properties such as the ability to account for changing ambient operational conditions. These alternative nozzle designs as well as the standard configuration will be elaborated upon further in the following subsections. [1,2]

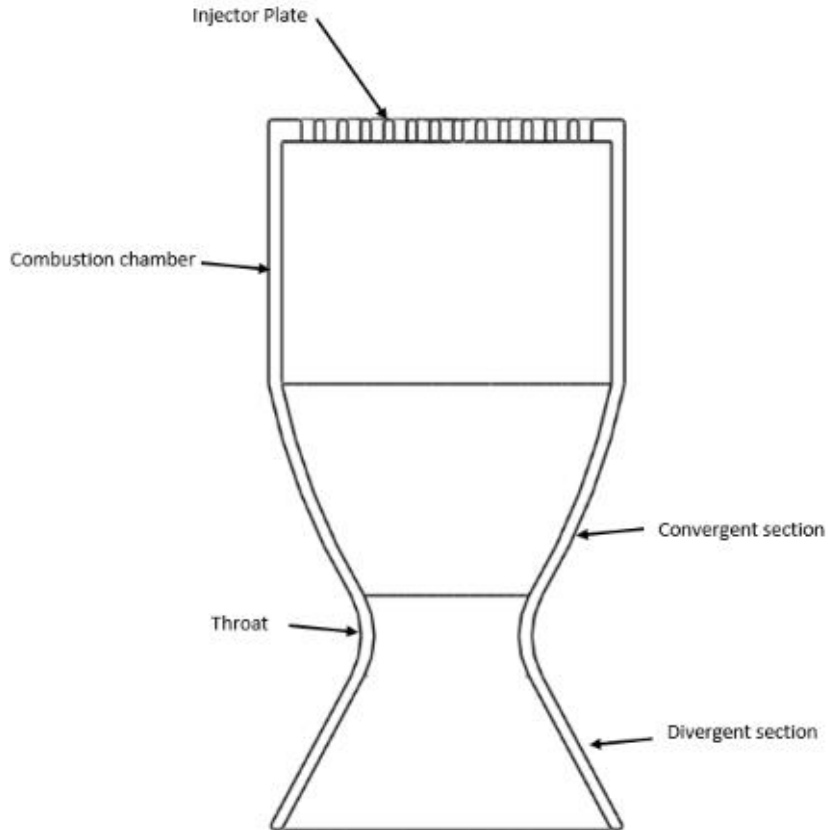


Figure. 1.1: Contemporary rocket nozzle configuration

1.3.1 De Laval rocket nozzles

Conventional De Laval or convergent-divergent nozzles are relatively well known and easy to design and implement in a rocket engine. Consequently, this nozzle type sees use in practically all contemporary rocket systems. However, De Laval nozzles have significant limitations in their performance during the ascent of the rocket owing to their fixed geometry [1,3]. As the rocket ascends and the ambient pressure surrounding the rocket decreases, the expansion of the exhaust gasses changes. This means that a De Laval nozzle can only operate at peak capacity at a specific operating pressure. Once the ambient pressure becomes lower than the nozzle exit pressure the flow becomes under expanded. When the flow is under expanded the flow results in a further expansion of the exhaust gases behind the rocket, inducing performance losses. Conversely, in the opposite case where the ambient pressure exceeds the nozzle exit pressure, oblique shock waves form at the exit into what is commonly referred to as a 'Barrel Shock' and the flow detaches from the divergent section of the nozzle walls. The exhaust plume is pinched by the greater ambient pressure reducing the efficiency of the engine and introducing dangerous instability into the system.

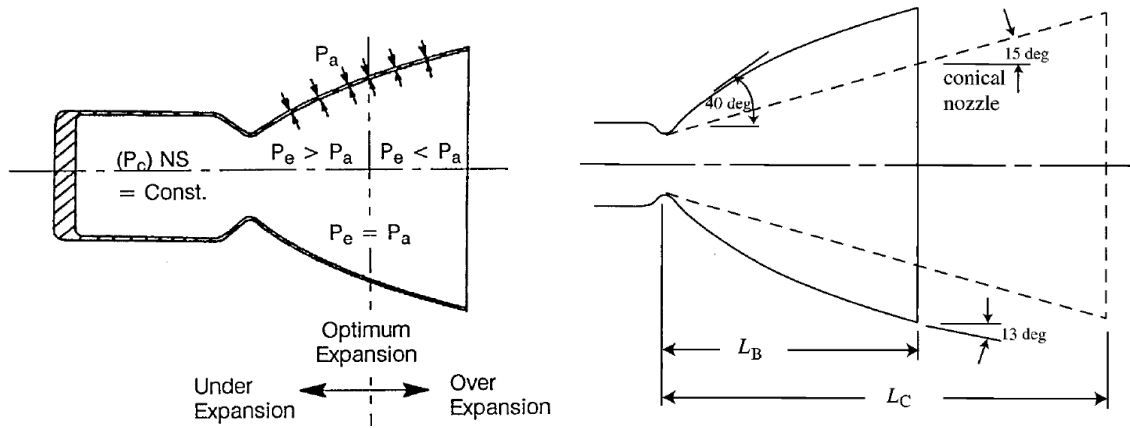


Figure. 1.2: Expansion properties of a De Laval nozzle [1]

1.3.2 Aerospike rocket nozzles

The concept of an aerospike nozzle was introduced to the aerospace community during the early 1960s. However, they have seen little development since the inception of the design due to the dominance of De Laval nozzles and associated difficulties of development. Despite this, aerospikes stand to perform much more efficiently than convergent-divergent nozzles owing to the inherent altitude compensating characteristics of the aerospike exhaust flow without the need to implement variable geometry. This passive altitude compensation means that such an engine maintains the expansion ratio at the theoretical ideal regardless of altitude and ambient pressure. This constant perfect expansion is achieved through the aerodynamic boundary formed by the ambient conditions relative to the flow of the nozzle, such that the expanding gas will flow radially outward through the toroidal exit and expand inward toward the spike geometry. The flow is subsequently exposed to the ambient conditions which result in the expansion becoming dependent on the ambient pressure [1,4,5].

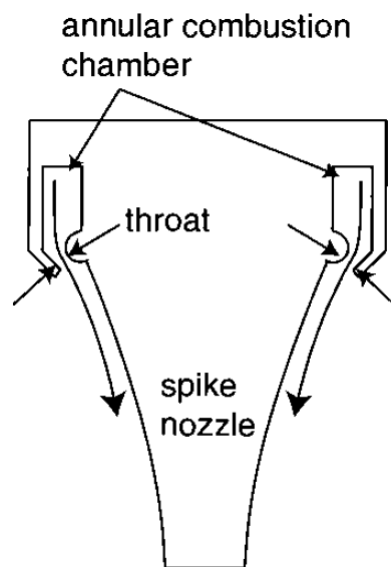


Figure. 1.3: Toroidal aerospike nozzle configuration [1]

Aerospike nozzles come in two varieties, the first being of a linear configuration with which the exhaust flow is directed along an elongated ramp that is symmetrical about its y-axis. The linear configuration relies on several separate combustion chambers directed toward the ramp geometry to achieve thrust. In the case of the second variety, the toroidal configuration (depicted in figure 3 above) expands the flow toward an annular center body. The toroidal variety exhibits an annular-shaped combustion chamber and throat. This throat is created by a cowl that surrounds the spike center body and acts as the outer wall of the combustion chamber as well as determining the exit diameter and “expansion ratio”. [1,6]

Figure 4 below illustrates the flow phenomena of toroidal aerospike nozzles with full-length center bodies at different off-design pressure ratios that were observed in experiments and numerical simulations [3,7,8]. In the case of pressure ratios higher than the design pressure for an aerospike, the exhaust flow expands near the center body without separation. In this case, a series of expansion and compression shocks forms in the exhaust flow. The characteristic Mach diamond formation is a result of the interactions between these shocks and the slip line. When the ambient pressure reaches the intended design value the flow characteristics will be that of a straight line traveling along the aerospike center body contour. In addition, the slip layer is parallel to the centerline. However, it is important to note that achieving these one-dimensional flow characteristics with a toroidal aerospike often cannot be achieved as the nonhomogeneous flow and expansion waves present in the throat region (a portion of the flow that is not considered in the center body design process) influence the exit flow profile. In the case of ambient pressures that are lower than that of the design pressure, the slip layer expands out with the ambient pressure allowing for “adaptation” to the changing conditions of increasingly lower pressures at higher altitudes.

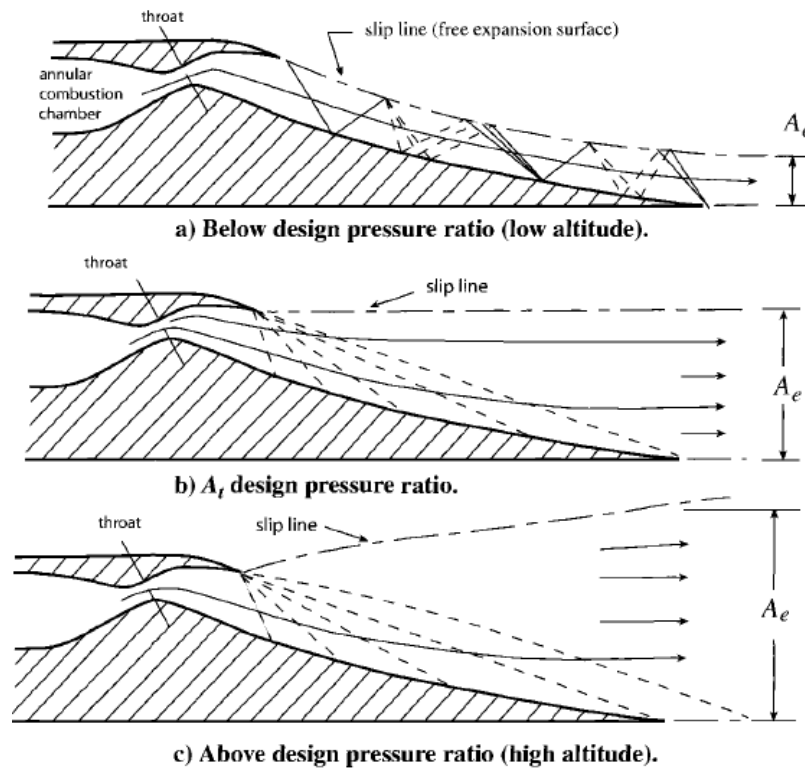


Figure. 1.4: Exhaust flow/expansion characteristics of aerospike nozzle [1]

Aerospike nozzle center bodies are often truncated which provides the advantages of reducing the considerable length and high structural mass of an appropriately countered center body. This truncation results in different flow characteristics in comparison to a full-length counterpart. When the ambient pressure present is high, an open wake flow establishes in the exhaust aft of the truncation with a pressure equal to that of the ambient pressure. In the case that the pressure is close to the design pressure, the base flow changes its characteristics and becomes closed-form. This is characterized by a recirculation zone that exhibits a constant base pressure that is no longer influenced by ambient conditions. Previous studies indicate that highly truncated center bodies trigger an earlier change in wake flow at pressure ratios below the design pressure ratio [1,2,4,5,9,10]. At the point at which the pressure within the wake becomes lower than the ambient pressure, the pressure within the closed wake remains constant. At these lower ambient pressures, the base pressure becomes higher than the ambient. This results in a net positive thrust contribution corresponding to the total base area. Figure 5 below depicts the various states of truncated aerospike flow discussed.

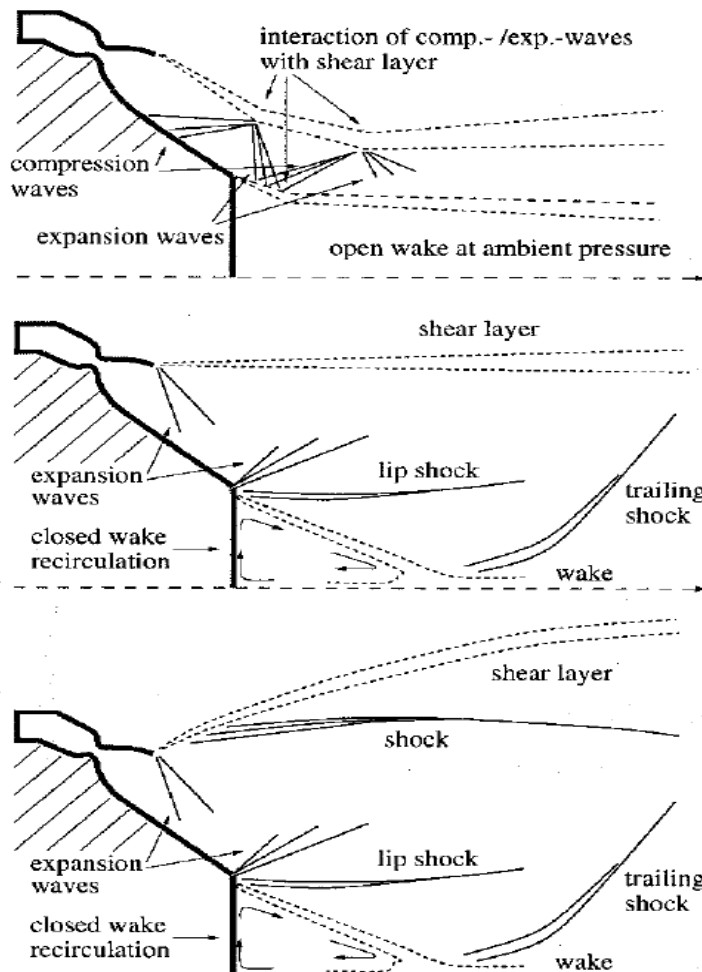


Figure. 1.5: Anatomy of truncated aerospike nozzle flow. [1]

1.3.3 Dual Throat nozzles

Apart from aerospikes nozzles, several unconventional configurations of nozzles have been investigated to overcome issues surrounding fixed expansion geometry. One such nozzle is the dual throat nozzle in which the fuel is ignited and burned within two concentric combustion chambers. When operating under a low altitude, the inner and outer combustion chambers operate simultaneously. During this operational mode, the engine has a larger throat providing a moderate expansion area ratio. Over the duration of its operation, at higher altitudes and lower ambient pressures, the outer thrust chamber is shut off and operation continues with only the inner chamber. In this mode of operation, the flow from the inner nozzle expands and attaches supersonically to the divergent portion of the outer nozzle. This results in a higher expansion area ratio for the remainder of the operation of the engine [1]. Figure 6 below details the flow characteristics of one such dual throat configuration.

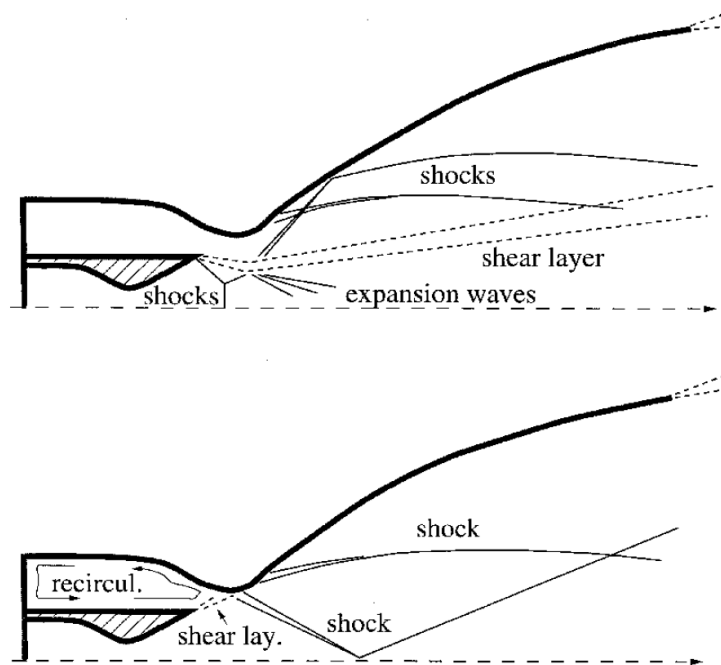


Figure. 1.6: Dual throat nozzle flow at sea level and high-altitude operation [1]

1.3.4 Combustion cycles

The means of supplying the fuel and oxidizer to the combustion chamber and nozzle of the associated engine is an integral part of rocket design which dramatically impacts the function of the rocket as a whole. There are many means by which to accomplish the goal of supplying the propellants and these are referred to as combustion cycles. For chemical rockets, most large-scale rockets utilize variations of the gas-generator cycle. This cycle siphons a portion of the propellant into a turbine-powered pump and combusted. The products of this secondary combustion drive the turbine and subsequently pump the corresponding propellant into the combustion chamber of the engine. Once the gases pass through the turbomachinery, they are exhausted downstream of the nozzle throat. An illustration of this process can be found in figure 7 below. Some performance is lost through this process as not all of the propellant is combusted and expanded through the primary nozzle. [1,11]

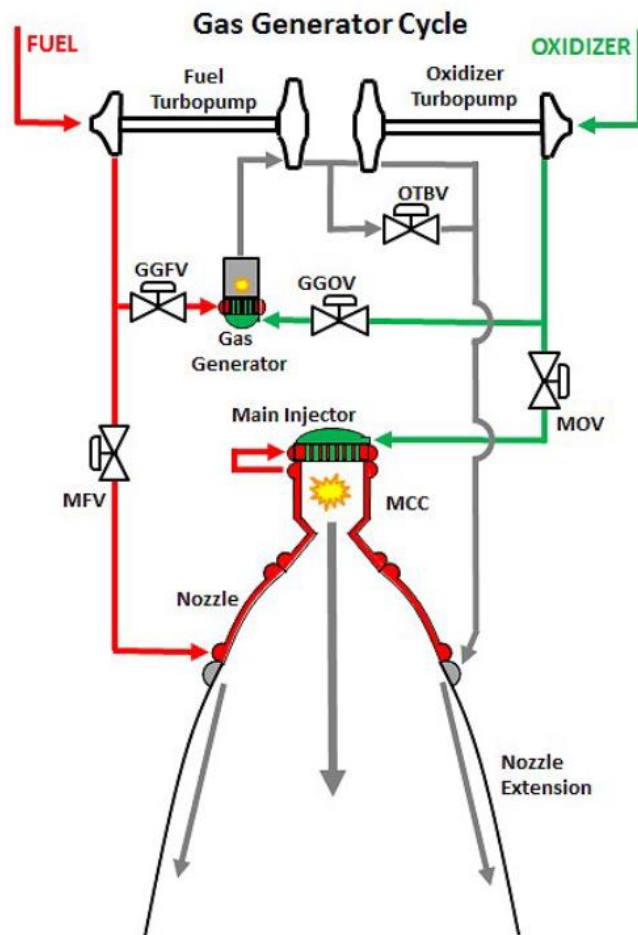


Figure. 1.7: Gas generator cycle [11]

One of the primary variations of the gas generator cycle is that of the closed expander cycle. In this cycle, the propellant is pumped through the regenerative cooling channels present in the nozzle. These channels transfer heat to the propellant where it becomes supercritical. The propellant is subsequently run through the turbopump and provides the necessary energy to run the cycle. [11]. As the propellant is driven across the turbine, they impart the energy necessary to run the cycle, before being injected into the thrust chamber. The expander cycle is considered a closed cycle as the entirety of the propellant passes through the main combustion chamber. However, the square-cube law limits this type of combustion cycle. The total cooling volume of the propellant increases faster than that of the useful conduction surface area. Simultaneously this increases the amount of energy required to operate the turbopump. This correlation limits the size of engines that incorporate this cycle.[11]

The last of the combustion cycles covered by this paper is that of the staged combustion cycle. In which either the fuel or the oxidizer is run through a pre-burner and partially ignited with a small amount of its counterpart. The exhaust gases and the unburned fuel flow then drive a turbopump and are subsequently ignited in the main combustion chamber. The primary drawback of this cycle is the mechanical complexity of the associated components adding greater

room for system error as well as overall mass, reducing reliability and the thrust to weight ratio. Figure 8 below illustrates this cycle in operation [11].

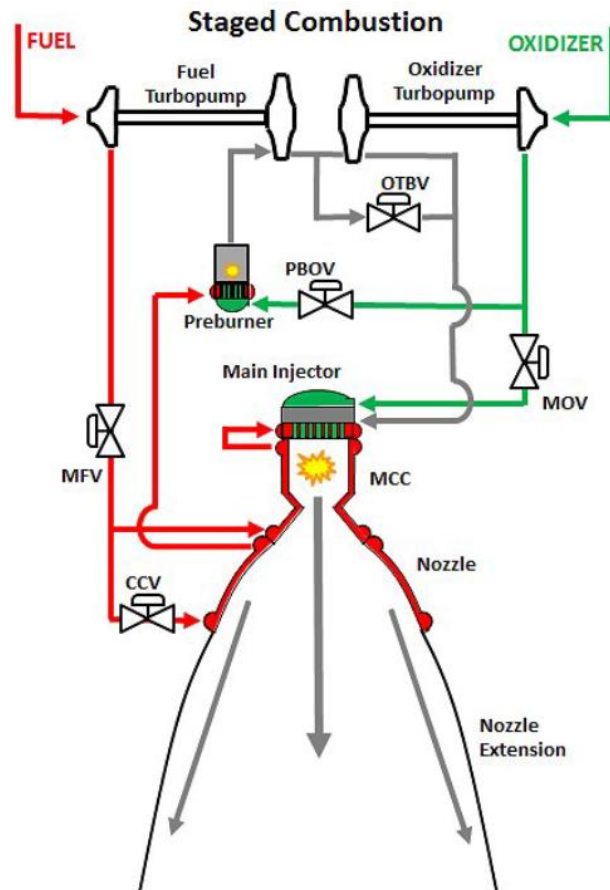


Figure. 1.8: Diagram of a staged combustion cycle [19]

1.4 Methodology

Due to the novelty of the system configuration and the unknowns associated with the interactions of the individual thrust chambers, the bulk of the study performed in this document will be through the use of computational means. Specifically, it will be broken down into three parallel approaches. The first will be that of a top-level systems design approach to account for the critical systems to be included with the novel engine design. The second will involve the design of the physical characteristics of the nozzle through the utilization of both classical convergent-divergent nozzle design methodology and that of an aerospike geometry approximation method developed by Gianfranco Angelino in 1964 [2,6]. The third and final approach will be the use of computational fluid dynamics in the form of ANSYS fluent, two-dimensional axisymmetric simulations to characterize and determine the performance and flow characteristics of the compound nozzle. This will be done at varying ambient pressure conditions in order to determine what effect each alternate expansion mode of the concentric nozzles with having on one another throughout the operation. This will be done for both dual throat operation and single throat operation for each mode respectively.

2. Intended System Purpose

The compound engine and associated systems are intended for the utilization of sample return missions between the inner solar system planetary bodies, specifically that of Mars sample return missions, and providing returning SSTO capabilities from the Martian surface. This provides the advantage of reducing the need for multiple successive stages and reduces system complexity. With the inclusion of a definite system purpose the subsequent design and analysis can be focused in scope while demonstrating overall system utility. Consequently, the following design and system analysis of the compound engine will be done in consideration of a Mars sample return mission.

2.1 Nozzle application

The design of the compound nozzle is intended to make up for the shortcomings of conventional rocket engine systems while simultaneously minimizing the complexity and associated costs. Consequently, the three alternate operational modes of the nozzle are intended for use as a second stage application in interplanetary missions allowing for SSTO capabilities in lower gravity environments found on planetary bodies such as Mars. More specifically, this nozzle design can be utilized for Martian sample return mission profiles as its use would eliminate the need for a secondary stage/launcher platform for a vehicle sent to the Martian surface, thereby reducing cost and mission complexity.

2.2 Mission profile

As discussed with the intended application of the design, the mission that will be used to analyze and design the new Compound engine system will be a short-term MSR mission. Consequently, this will consist of four phases. With the first of these phases being the ascent to low earth orbit through the use of an appropriate launch platform. The second phase involves the departure from LEO to the Martian surface. The third phase includes the collection of the desired samples and other scientific activities as well as the departure from the Martian surface to LMO. The fourth and final phase of the mission involves leaving the orbit of Mars to touch down on earth at the desired location. A simplified scale view of the path taken through this mission profile is illustrated in Fig. 9. Below

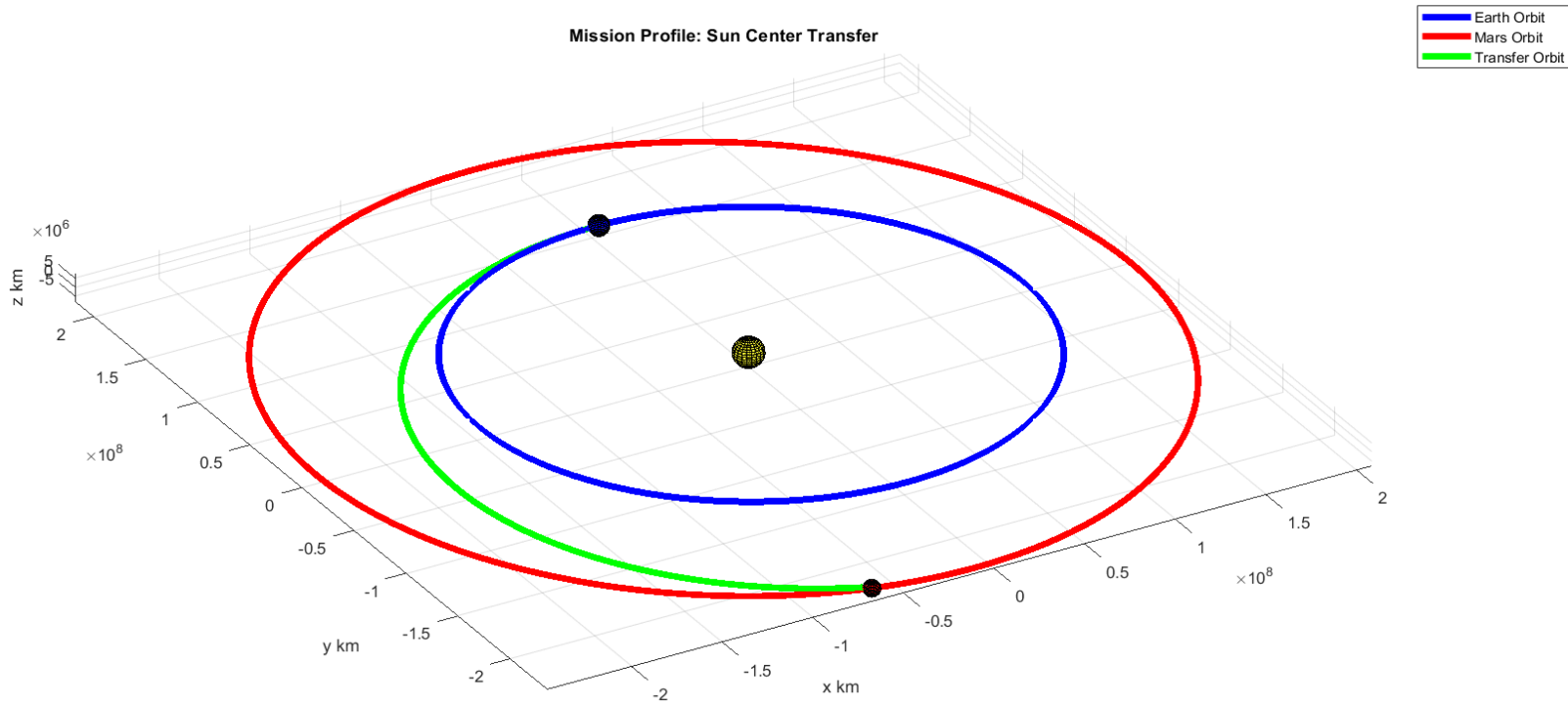


Figure. 2.1: Visualization of theoretical mission profile [2]

The purpose of introducing SSTO capabilities with respect to Martian operations that this functionality would allow for the reduction in additional craft complexity and waste, with the compound engine serving to make up for the traditional shortcomings of such an operation mode. Consequently, the foreseeable cost of such an endeavor would be reduced and allow for more frequent rendezvous with the red planet.

In order to design the spacecraft for this mission profile, relevant examples and prior missions were examined and compared. A similar design requirement to that of the 2020 Perseverance rover mission was noted and utilized as a reference mission profile. As this study focuses on the second stage of such a system the Centaur III will be used as the system design benchmark.

Table 2.1: Centaur III specifications

Centaur III Second Stage Rocket	
Engine	RL-10
Fuels	Liquid Oxygen & Liquid Hydrogen
Combustion Cycle	Expander Cycle
Specific Impulse	373-470s
Thrust	101.9 KN
Length	12.6 meters
Diameter	3 meters

An additional advantage of the Perseverance mission benchmark is the specification of the mass limitations/requirements for each stage and the associated metrics. Therefore, with the acceptable mass of our payload at a maximum of 1050 kg and that a total of 10.49 Km/s of delta-V is necessary for a 1.2 year-round trip between the earth and mars (depicted in image 10 below), an appropriate change in velocity was chosen each of the phases to focus on the performance metrics required out of the proposed system. Thus, allowing for the focus on the propulsion system's design and system layout.

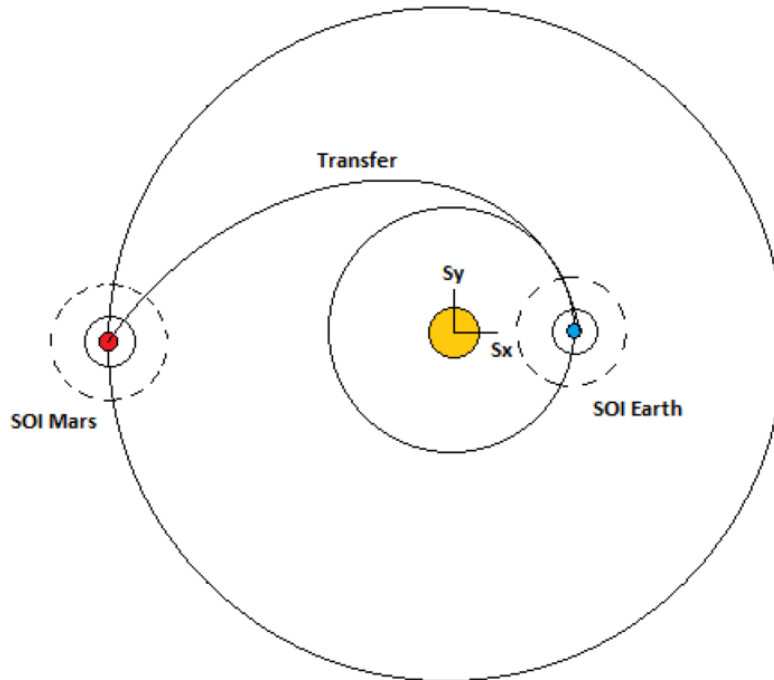


Figure. 2.2: Earth to mars Hohman transfer

Simulation of the mission profile was completed with the utilization of MATLAB to construct a series of two-body problems that could be utilized to specify the necessary delta-V for the transfers incorporated into the mission profile. This code (which is listed in the appendix of this document) takes into account several assumptions to simplify the problem, these assumptions are listed as follows.

- Patched-conic approximation
- Spacecraft trajectory is partitioned into two-body segments.
- Motion during each orbit segment is dominated by a single sphere of influence relative to the nearest relevant celestial body.
- Orbits and propagation are kept as restricted 2-body problems
- Earth and Mars are in near-circular heliocentric orbits

With these assumptions, the total delta-V required for the propulsion system to conduct an interplanetary trajectory burn from Earth to Mars utilizing a Hohmann transfer was calculated. Consequently, it was calculated that a delta-V of 3.65 km/s would be required to boost and accelerate the associated spacecraft from low earth orbit into a transfer ellipse around the sun. This value is consistent with similar values established in associated literature.

In order to enter the vessel into a low orbit about mars, an additional burn yielding a delta-V of 3.19 km/s is required. This results in a total delta-V of 10.49 Km/s for the mission profile under a round trip transfer paradigm. The time elapse associated with this transfer was calculated to be approximately 278.5 days. The constants associated with these calculates are tabulated in table 2 below.

Table 2.2: Mission profile constants

Orbit Constants				
Body	Mass (kg)	GM (km ³ /sec ²)	Radius (km)	Distance to Sun (km)
Earth	5.972 x 10 ²⁴	398,332	6,378	150,000,000
Mars	6.4169 x10 ²³	42,800	3,389	211,339,054
Sun	1.989 x10 ³⁰	1.327 x10 ¹¹	695,800	N/A

3. Nozzle system design

As mentioned previously, the nozzle of any rocket engine is responsible for accelerating the propellants and imparting thrust to the entire system. Consequently, the maximizing performance and functionality of the nozzle is paramount. However, there are fundamental limitations of contemporary rocket nozzle designs. These limitations are, that the changing ambient conditions affect the expansion and performance of the engine and the nozzle's inability to be of use in more than one operational mode, in tandem these factors significantly hamper engine performance. Ultimately these limitations place a ceiling on the capabilities of conventional rocket engines that necessitates the development of alternative propulsion systems.

3.1 Nozzle profile

The compound nozzle design is separated into three components for the purpose of this paper. Those components are, the truncated aerospike nozzle design, the De Laval nozzle design, and the integration of both into the dual throat configuration respectively. The following sections detail the design of both nozzles, the combination of each, and the subsequent integration into the overall combustion cycle.

3.2 Annular nozzle design

The Aerospike nozzle has three primary components. The cowl, support structure, and the center body respectively. The space between the cowl and the center body constitutes the throat of the nozzle. From the theoretical throat position relative to the cowl, the contour of the center body ramp can be calculated. This was done by utilizing the approximation method developed by Gianfranco Angelino [12]. This is accomplished by considering a series of isentropic expansion waves that are generated at the tip of the cowl. These expansion waves increase the velocity of the flow toward the center body and change corresponding to the ambient pressure conditions. Following this, it is assumed that the flow is parallel to the nozzle axis at the exit. Through the associated equations below, the center body contour aft of the cowl is given as a series of points for a given expansion ratio, ϵ .

$$\theta_t = \nu(M_e) \tag{3.1}$$

$$\nu = \sqrt{\frac{\gamma + 1}{\gamma - 1}} \tan^{-1} \sqrt{\frac{\gamma - 1}{\gamma + 1} (M^2 - 1)} - \tan^{-1} \sqrt{M^2 - 1} \tag{3.2}$$

$$\begin{aligned} A_t &= \pi(r_e^2 - r_t^2) / \cos \theta_t = \frac{F}{p_c C_F} \\ A_e &= \pi(r_e^2 - r_t^2) \end{aligned} \tag{3.3}$$

$$r^2 = r_e^2 - (r_e^2 - r_t^2) \frac{A \sin(\mu + \theta)}{A_t \sin \mu \cos \theta_t} \quad (3.4)$$

$$x = \frac{r_e - r}{\tan(\mu + \theta)} \quad (3.5)$$

$$\frac{A}{A_t} = \frac{1}{M} \left[\frac{2}{\gamma + 1} \left(1 + \frac{\gamma - 1}{2} M^2 \right) \right]^{\frac{\gamma + 1}{2(\gamma - 1)}} \quad (3.6)$$

A 2-D illustration of the aerospike center body is shown below in Fig. 11. The figure includes the major variables present in the center body along with a representation of a spike truncation. Such a truncation of the center body length provides several benefits. Namely, the reduction in length corresponds with a reduction in the weight of the system. This also eliminates the need to cool the farthest end of the spike allowing for more adequate cooling. The potential losses from the removal of a portion of the center body contour are offset by a recirculation zone of the flow that acts as a virtual center body tip. Relevant to this is that several studies have yielded the metric that significant losses only began to occur in designs with truncations beyond that of 60% [1,6,13].

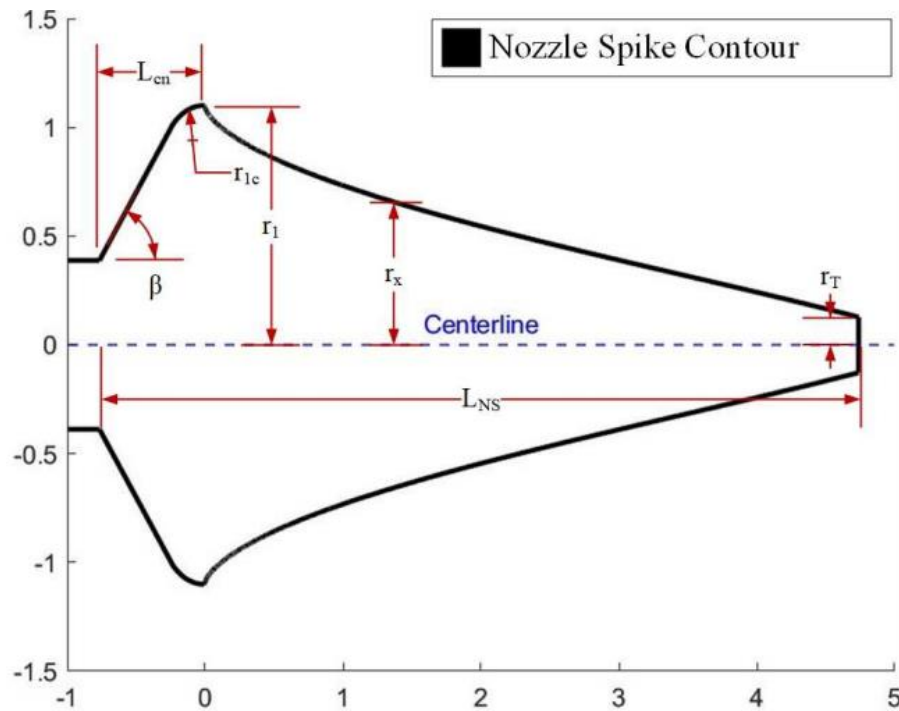


Figure. 3.1: Aerospike nozzle contour dimensions [2]

The aerospike cowl works in conjunction with the center body to accelerate the combusted propellants in quasi-one-dimensional flow. The throat location is defined as the angle between the endpoint of the cowl and the closest point along the center body relative to the formation of the expansion waves defined as θ_t . An illustration of this relationship is shown in image 12 below. The design of the nozzle geometry prior to this throat is determined by two factors. The first is a reflection of the ramp geometry to account for the “convergent” section of the center body. While the second is necessary alterations to the integration of the support structure and interior nozzle.

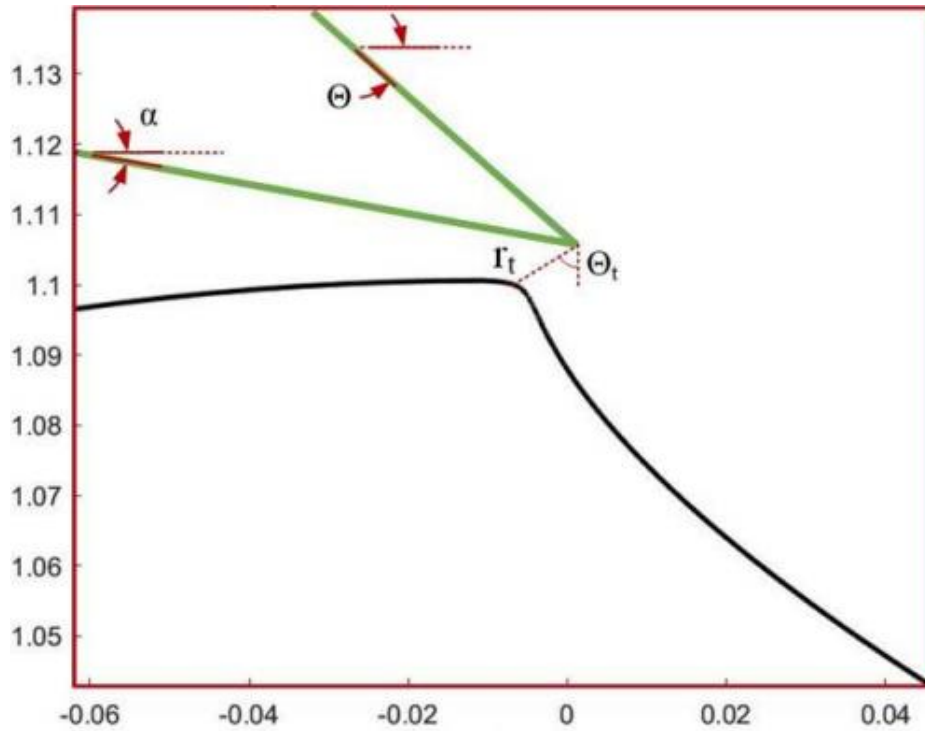


Figure. 3.2: Cowl to center body relation variables [2]

Utilizing the aforementioned methodology and calculations for the aerospike nozzle design, a MATLAB code was created to calculate the geometry of the aerospike ramp geometry as well as the associated throat/cowl position. The results of this calculation are detailed in the following table (table 3) along with a visual representation of the nozzle contour graphed in figure 13 below. The center body spike is later truncated to roughly 40% of its original length in the integration of the center nozzle.

Table 3.1: Derived values for aerospike

Aerospike characteristics	
Distance from spike to cowl	0.0385 m
Total Length	3.0427 m
Chamber Temperature	2760 K
Chamber Pressure	2.4 Mpa
Throat Area	0.1982 m ²
Exit Area	1.9598 m ²
Area Ratio	10.356
Theta t	65.1192

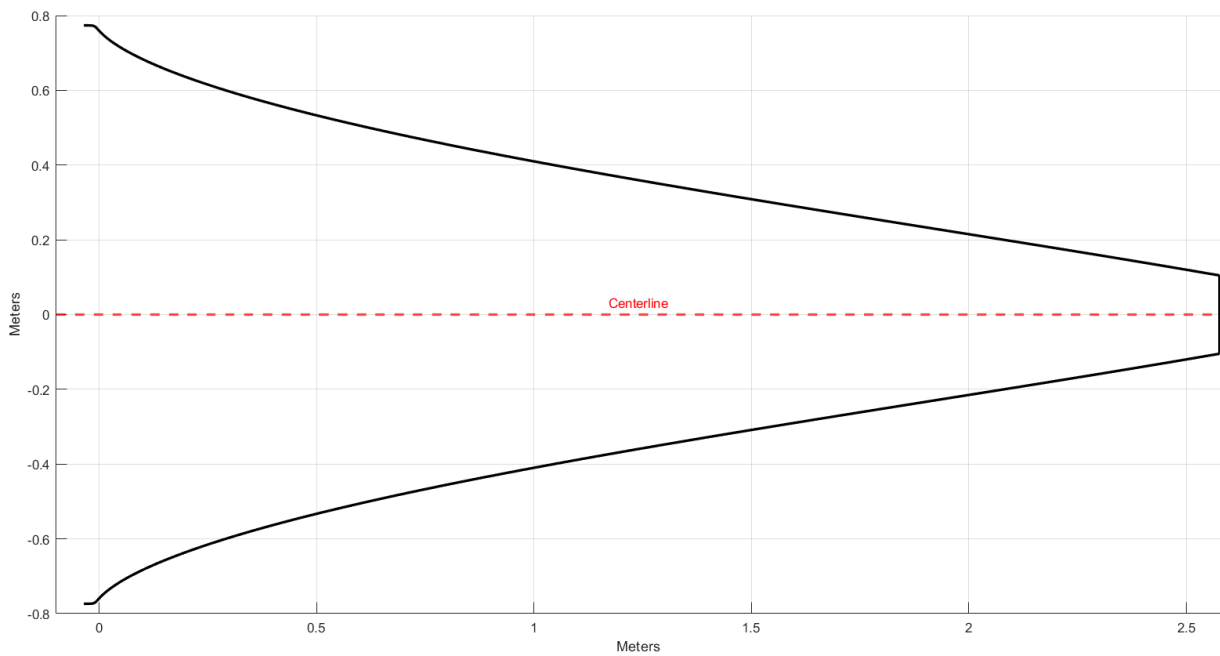


Table 3.2: Aerospike center body contour

$$V_{eq} = v_e + \frac{(p_e - p_a) \cdot A_e}{\dot{m}} \quad (3.7)$$

$$\Gamma(\gamma) = \sqrt{\gamma \cdot \left(\frac{1+\gamma}{2}\right)^{\frac{1+\gamma}{1-\gamma}}} \quad (3.8)$$

$$\frac{A_e}{A^*} = \frac{\Gamma(\gamma)}{\sqrt{\left(\frac{2\gamma}{\gamma-1} \cdot \left(\frac{P_e}{P_c}\right)^{\frac{2}{\gamma}} \cdot \left[1 - \left(\frac{P_e}{P_c}\right)^{\frac{\gamma-1}{\gamma}}\right]\right)}} \quad (3.9)$$

$$v_e = \sqrt{\left(\frac{2\gamma}{\gamma-1} \cdot \frac{R}{M_w} \cdot T_c \cdot \left[1 - \left(\frac{P_e}{P_c}\right)^{\frac{\gamma-1}{\gamma}}\right]\right)} \quad (3.10)$$

$$F_T = \dot{m} \cdot V_e + (P_e - P_a) \cdot A_e \quad (3.11)$$

Design of the interior nozzle was corroborated utilizing the software Rocket Propulsion Analysis, a program that facilitates the design and analysis for conventional engine profiles. Several iterations of the interior nozzle were designed corresponding the performance results of the compound configuration yielded by the computational analysis detailed later in this document. At the end of this process a final nozzle design was obtained. The relevant metrics associated with the nozzle design as well as the contour/nozzle geometry derived from this process are detailed in table 4 and figure 15 below.

Table 3.3: Thrust and mass flow rates of inner nozzle

Thrust and mass flow rates	
Specific impulse	394.41533 s
Chamber thrust	82.02829 KN
Total mass flow rate	21.18514 kg/s
Oxidizer mass flow rate	17.85157 kg/s
Fuel mass flow rate	3.85257 kg/s

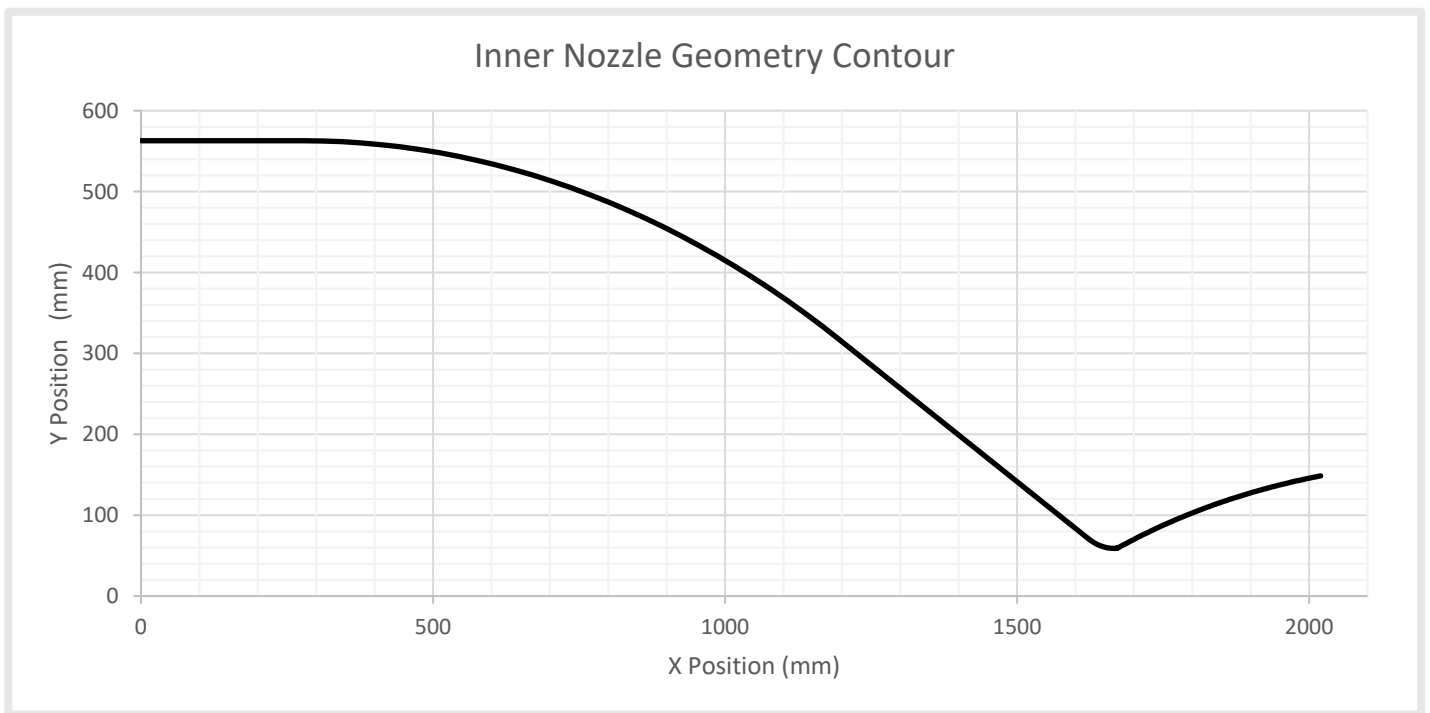


Figure. 3.4: Convergent divergent nozzle contour

3.4 Dual throat configuration

The dual throat configuration of the aerospike and the De Laval nozzle represents the integration between each of the respective systems. This is done, such that the contoured nozzle sits within the center body of the aerospike with its exit diameter matching that of the truncation diameter the spike geometry. In this orientation the engine consists of two separate combustion chambers with the annular aerospike chamber surrounding the conventional chamber of the contoured nozzle. This allows for three modes of operation the first being the firing of both nozzles and combustion chambers simultaneously, while the second and third are the single firing of the outer aerospike and the inner contoured nozzle respectively. The potential benefits of this configuration being the ability to control the ambient pressure and expansion conditions surrounding the inner contoured nozzle through the passive altitude compensating flow of the surrounding aerospike nozzle.

Over the course of the design process detailed in this document, several iterations of the nozzle configurations were constructed. The first initial design configurations consisted of a both a sea level optimized, and vacuum optimized de Laval nozzle integrated into the center body contour of the aerospike truncation. This was done to establish endpoint baselines for nozzle configuration performance and determine the appropriate inner nozzle design parameters for a completed design. Consequently, a third and final configuration, incorporating lessons learned from the initial iterations was utilized for further analysis. Illustrations of the initial configurations and the final configuration are depicted in figures 16 and 17 below respectively.

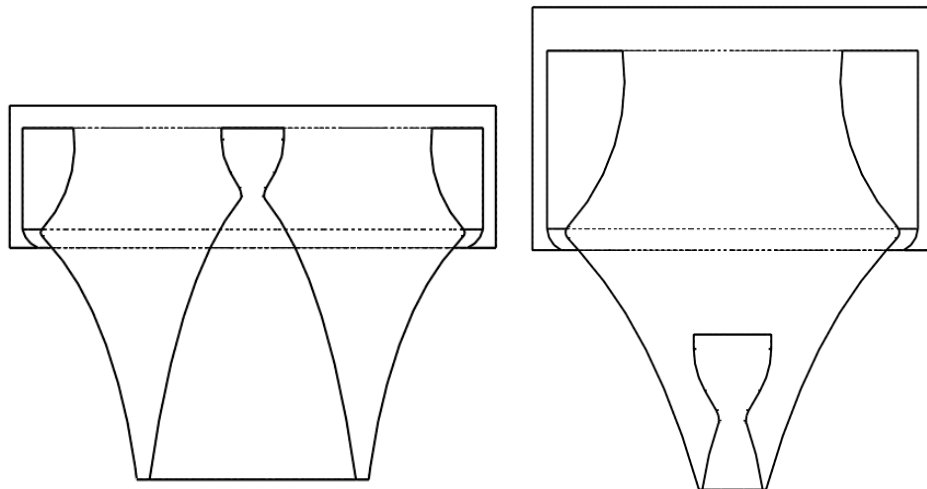


Figure. 3.5: Illustration of initial compound nozzle iterations

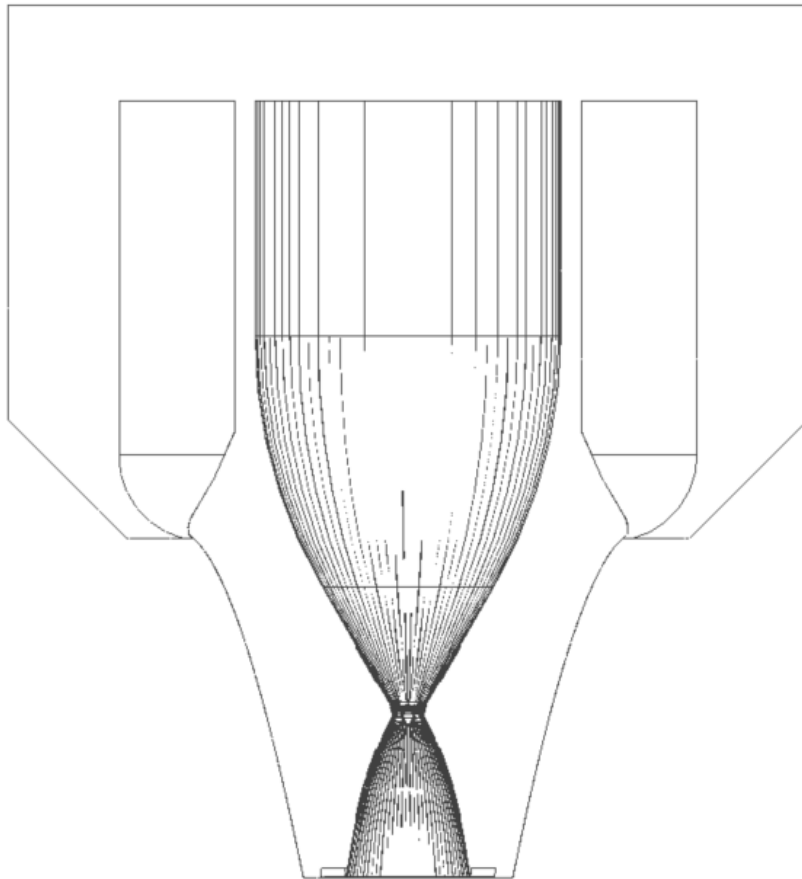


Figure. 3.6: Final compound nozzle configuration

4. Combustion cycle design

Due to the extreme temperatures present during the operation of a rocket, engines require a means to mitigate the negative effects these temperatures have on the integrity of the system. This represents the main objective of the cooling system as if the engine structure becomes too hot, it will no longer be able to withstand the pressures associated with operation. As stated previously, in the case of an expander cycle the coolant system serves the secondary purpose of driving the turbopumps.

As the temperature is increased most materials lose their advantageous structural properties and become weak. Sustained exposure to such temperatures will result in failure or even melting. To combat this issue most conventional engines are designed to utilize regenerative cooling, a process that takes advantage of the cryogenic propellants. This process allows for the thrust chambers of an engine to reach thermal equilibrium, limited only by the quantity of propellant remaining in the system.

4.1 Combustion cycle profile

As discussed in the literature review, the means by which the fuel and oxidizer are supplied is an extremely integral part of any engine design and one that is often underestimated in the engineering process. Commonly, turbine-powered pumps siphon some fuel to drive the main volume of fuel and oxidizer at the desired rate, while the fuel is fed through the bottom of the engine and used as a coolant to pass through regenerative cooling channels. This process however fails to take advantage of the sublimation of the fuel that takes place in the cooling channels. Expansion cycles on the other hand do utilize this phenomenon such that the sublimating fluid is used to drive the turbopump rather than a smaller sustained combustion. This has the added benefit of resulting in significantly lower stresses placed on the pump assembly, driving up reliability and reusability. Additionally, there is the added benefit that the cycle is closed and 100% of the propellant passes into the combustion chamber. These cycles are limited by the nozzle area in relation to pumped fuel volume. Figure 18 below illustrates the basic flow path of the fuel and oxidizer through a closed expander cycle. [12,13]

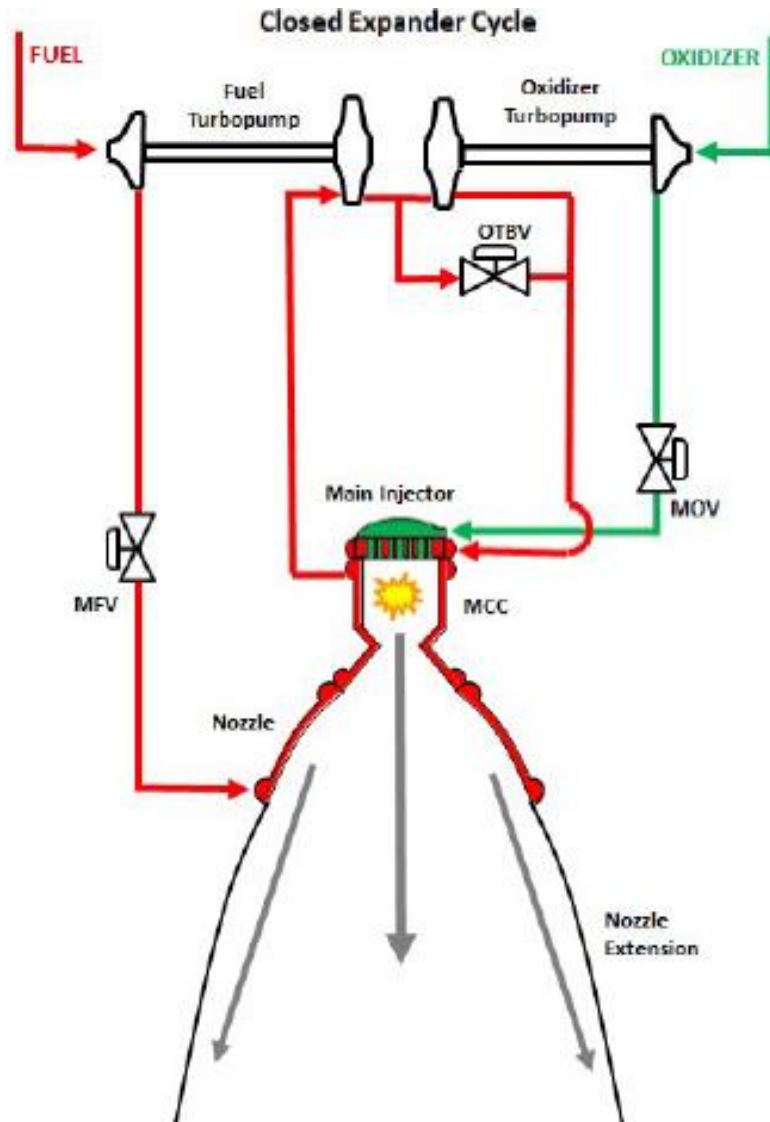


Figure. 4.1: Closed expander cycle [11]

Aerospike represents a good candidate for use in an expansion cycle due to the extreme heating seen by the center body geometry and the increased nozzle area. Further with the inclusion of the interior nozzle for the compound nozzle and the increased heat and area the expander cycle was chosen for the system design.

4.2 Combustion cycle architecture

With the Compound nozzle consisting of two concentric nozzles each with their own respective cooling requirements, the dual-expander cycle was chosen for its unique applicability to this system. A dual expander cycle utilizes both the fuel and the oxidizer to sublimate through the cooling system and provide power to two separate turbopumps, one for each combustion component. Normally this proves to be a difficult design challenge as it is critical that these components do not make contact prior to the injector plate, which in conventional engine

systems either requires complex plumbing or specially designed turbopumps with an inert gas barrier. With the Compound nozzle, the cooling of the inner and outer chambers can be delegated to either the fuel or the oxidizer such that they do not pass through the same plumbing prior to the desired point. Additionally, this cycle is made possible with the fuel of choice for the system being liquid hydrogen and the oxidizer liquid oxygen, as both of the propellants are cryogenic and able to provide significant cooling. [12,13]

The dual-expander cycle configuration allows for an increase in specific impulse when the outer combustor is firing with the inner shut down. This is especially advantageous for the Compound nozzle as its intended use is for operation in both atmospheric and vacuum conditions. There are, however, drawbacks to implementing this plumbing architecture with the nozzle. Specifically, the increased complexity of the nozzle design and aerospike center body will result in a relatively heavy configuration when compared to more conventional systems. This also necessitates an increased number of control valves throughout the system plumbing. A simplified plumbing and instrumentation diagram detailing the locations of the turbines and control valves is shown in figure 16 below. This diagram includes the path of both the fuel and the oxidizer. The fuel is driven by the fuel turbine through the inner nozzle where it becomes supercritical travels back into the turbine, powering it, and then through to the injection. Similarly, the oxidizer is driven by the Ox turbine and travels through the annular nozzle/cowl channels, goes supercritical, and powers the turbine where it is driven through to injection.

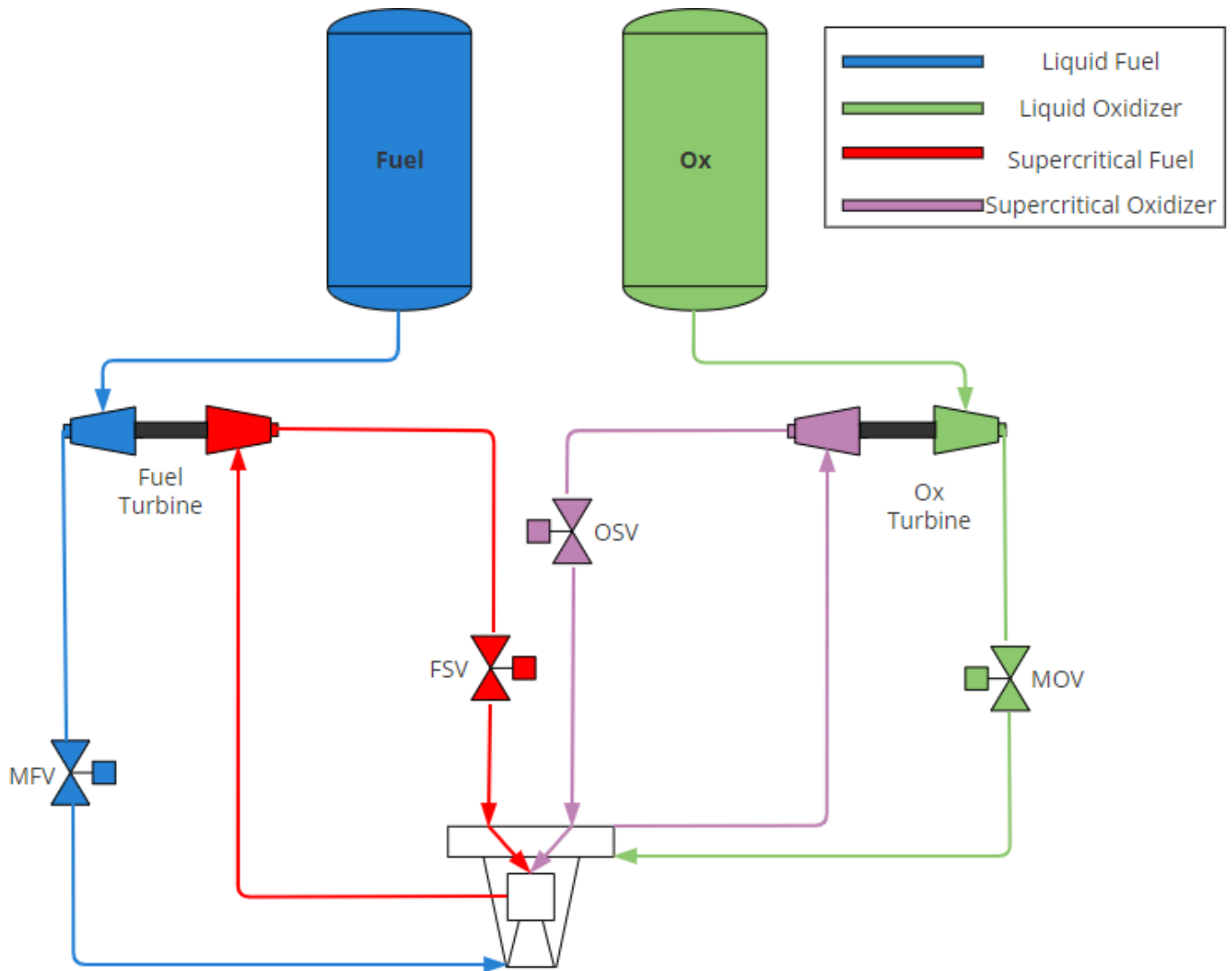


Figure. 4.2: Simple P&ID of dual expander cycle

4.3 Combustion cycle integration

The integration of the cycle and the compound nozzle involves each propellant acting as the coolant for an individual coolant path. Fuel is used for the inner convergent-divergent nozzle and center body, while oxidizer is for the aerospike cowl and annulus. Figure 19 above details the flow path through the nozzle itself. The mixture ratio of 4.5 was determined to produce the greatest specific impulse for the propellants and nozzle choices. [1] with the associated mixture ratio, the turbines supply the necessary mass flow rates to the corresponding nozzle manifolds. In the case of the center nozzle, the oxidizer flow rate required is 15.85 kg/s and the corresponding fuel mass flow rate is 3.52 kg/s. For the outer aerospike, the total mass flow rate required is 65 Kg/s.

5. Coolant system design

Due to the extreme temperatures present during the operation of a rocket, engines require a means to mitigate the negative effects these temperatures have on the integrity of the system. This represents the main objective of the cooling system as if the engine structure becomes too hot, it will no longer be able to withstand the pressures associated with operation. As stated previously, in the case of an expander cycle the coolant system serves the secondary purpose of driving the turbopumps.

As the temperature is increased most materials lose their advantageous structural properties and become weak. Sustained exposure to such temperatures will result in failure or even melting. To combat this issue most conventional engines are designed to utilize regenerative cooling, a process that takes advantage of the cryogenic propellants. This process allows for the thrust chambers of an engine to reach thermal equilibrium, limited only by the quantity of propellant remaining in the system.

5.1 Coolant system profile

Regenerative cooling is accomplished through the application of channels constructed into the walls of the rocket nozzle. One of the engine propellants, which is most commonly the fuel is fed through these channels from the base of the nozzle structure, traveling up the channels prior to injection through the injector plate. Figure 20 below illustrates the conventional manufacture and profile of the regenerative cooling channels in a rocket nozzle.

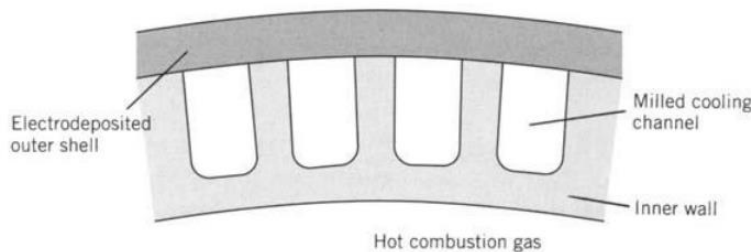


Figure 5.1: Regenerative cooling channel profile [22]

The heat absorbed through regenerative cooling is not considered waste heat, as it brings up the energy content of the propellant as it travels through the system and into the injector plate. This effectively results in an increase in the engine exit velocity by up to 1.5%. [22] The design of the cooling channels takes advantage of thin walls, reducing thermal stresses and aiding in heat transfer between the surface and propellant. This configuration additionally has the benefit of reducing the overall weight of the engine structure. The geometry of these channels plays a significant role in their effectiveness and will change diameter depending on the point along the nozzle contour to account for areas of exceptional heating such as the throat.

5.2 Coolant system decomposition

The heat transfer in a regeneratively cooled rocket nozzle can be simplified as the steady-state heat transfer between two fluids with a layered divider. Figure 21 below illustrates this

breakdown. Provided the assumptions illustrated in image # and a steady-state problem the following equations were utilized to characterize each respective coolant

$$h_{gc}(T_{aw} - T_{wg}) = q = \frac{k}{t}(T_{wg} - T_{wc}) \tag{5.1}$$

$$= h(T_{wc} - T_{co}) \tag{5.2}$$

$$= H(T_{aw} - T_{co}) \tag{5.3}$$

$$H = \frac{1}{\frac{1}{h_{gc}} + \frac{1}{k} + \frac{1}{h_c}} \tag{5.4}$$

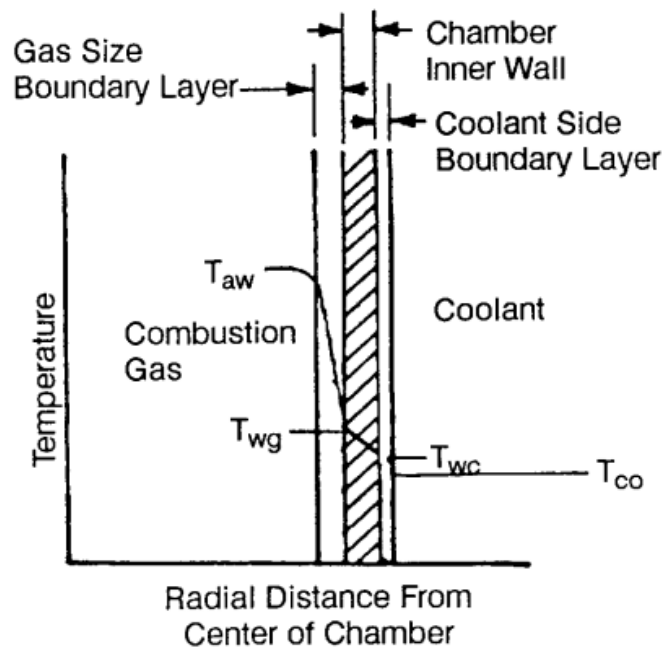


Figure. 5.2: Regenerative cooling heat transfer profile

5.3 Coolant system architecture

There are three design parameters that define the design of a regeneratively cooled rocket nozzle. Namely, the nozzle material's thermal conductivity, the thickness of that material, and the maximum operational temperatures. Materials with a high thermal conductivity represent the best choice for material selection as such materials see a reduction in wall temperature for a given heat flux. This effect is only advantageous to a point, should the temperatures outpace the cooling system's ability to compensate the material integrity will be compromised. The thickness of the nozzle material drives the structural strength to withstand the extreme pressure and

temperatures experienced by nozzle operation. Additionally, the thickness of the material will directly affect the pressure change requirements.

Taking these design parameters into account, as well as the added heat to the system driving the turbopumps regenerative cooling channels were included in the design of the compound nozzle center body and toroidal cowl. As stated in the chapter regarding the combustion cycle the design, both the fuel and oxidizer are utilized, fuel for the center body and oxidizer for the cowl assembly with each channel system independent of the other.

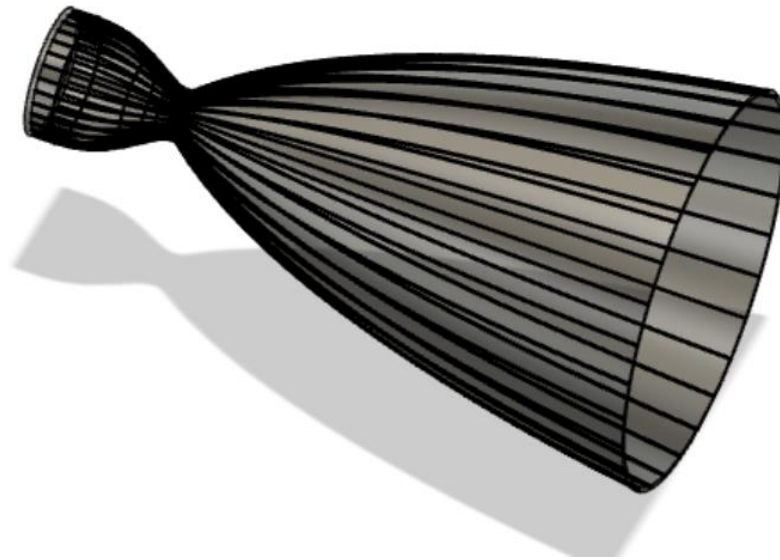


Figure. 5.3: Visual representation of Regenerative cooling channels in the center nozzle

Assuming the nozzle construction is that of NARloy-Z with a thermal conductivity of 290 W/mk, the channel size across the inner convergent-divergent nozzle was calculated to be a rectangular channel 1.5mm in width and 2.818mm in length. The total number of channels is 150. Each of these channels utilizes liquid hydrogen propellant and performs two passes across the length of the inner nozzle such that incoming fluid travels down the channels in the same direction as the combustion products until the end of the nozzle at which point the channels double back and travel against the flow of the combustion products up to the injector plate. Similarly, the channels utilizing liquid oxidizers utilize the same double pass flow path across the cowl of the outer annular nozzle. A representation of the final nozzle design with the regenerative cooling channels incorporated into the geometry is shown in figure 23 below.

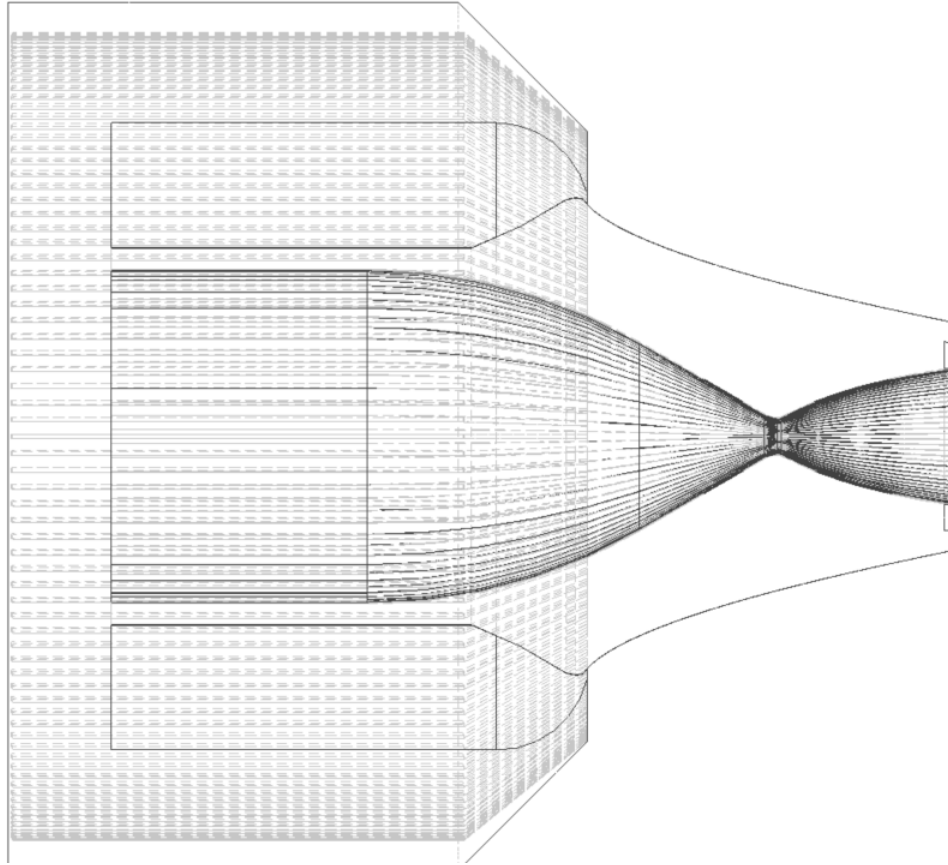


Figure. 5.4: Integration of double pass regenerative cooling channels into the compound nozzle

In addition to the design of the coolant channels, the temperature and heat flux across the inner nozzle was calculated through the use of RPA (Rocket Propulsion Analysis) such that the corresponding values were graphed with respect to the position in figures 24 and 25 below. The cooling of the center body is assumed to undergo a similar increase in temperature relative to position along its length. Consequently, the regenerative cooling channels for the center body exhibit the same number as that of inner as it passes up to the injector.

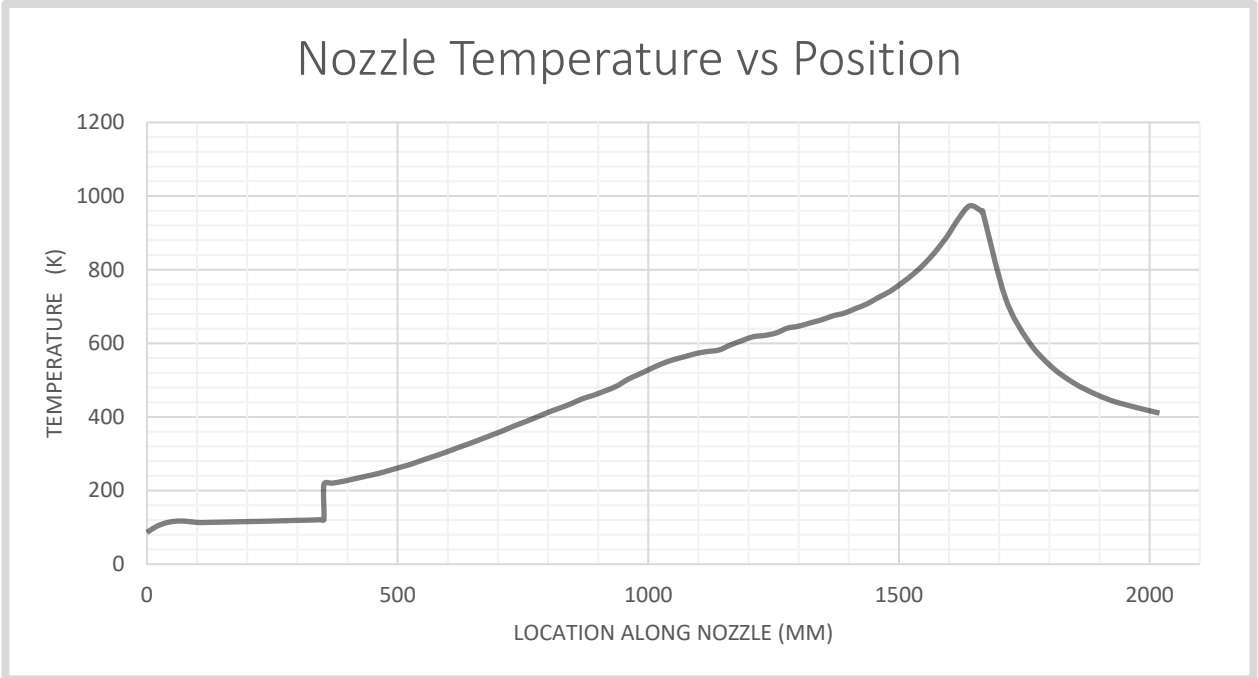


Figure. 5.5: Inner nozzle temperature relative to the position

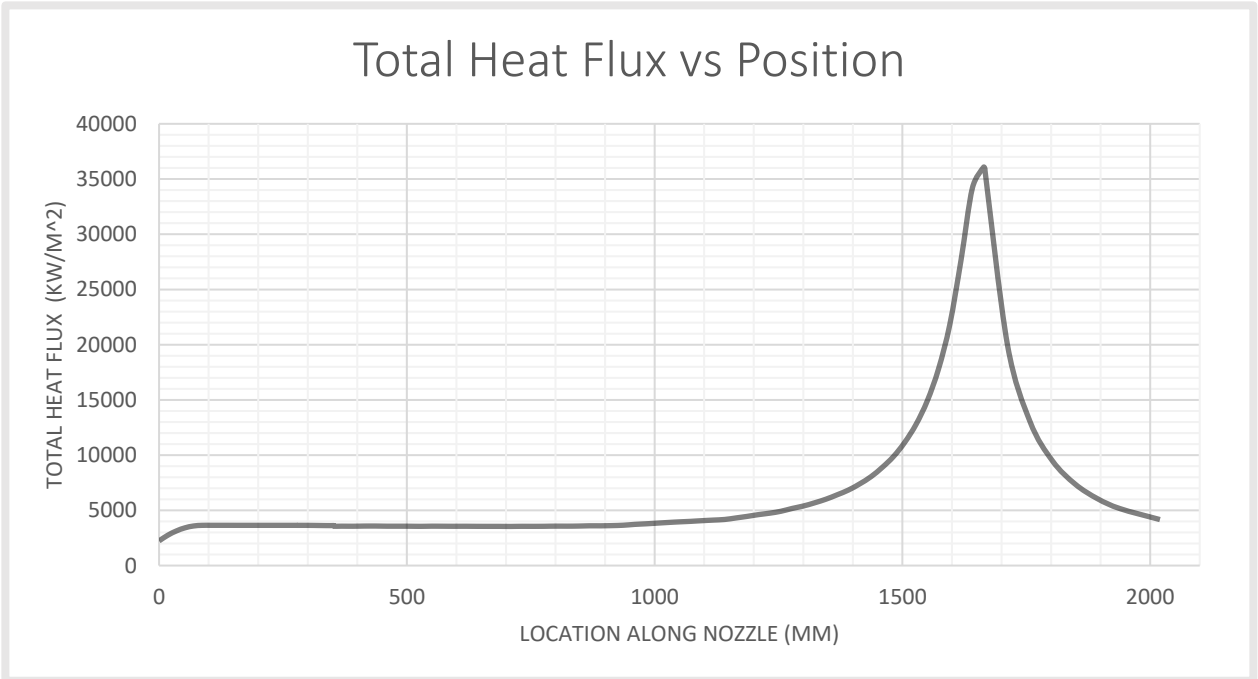


Figure. 5.6: Inner nozzle total heat flux relative to the position

6. Computational fluid dynamics analysis

To characterize the functionality of the novel compound nozzle design, the use of computational fluid dynamics or CFD was required. The CFD program Ansys Fluent, a fully featured solver for modeling flow and related physical phenomena was used. Several simplified models of each nozzle iteration were created and used to generate a 2-dimensional simulation of the accelerated propellant flow through the compound nozzle. This was done at all three of the associated operational modes, Annular, Convergent-Divergent, and Dual. Each simulation was set up as a steady-state pressure-based cross-section of the compound nozzle starting from the injector plate of the annular aerospace. Gaseous oxygen was set at a constant mass flow rate representative of the center channels at full throttle. the boundary conditions of the simulations were set as the following. The incoming pressure of the oxygen was set to be 4.6 megapascals at the inner nozzle while the annular nozzle was set to be 6 megapascals. Each of these inlets was set with an initial temperature of 300 degrees Kelvin. To account for the high compressibility and speed of the simulation, an axisymmetric density-based model was set under a K-epsilon RNG viscous regime.

The fluent simulations were constructed utilizing the nozzle contours calculated with the associated processes discussed in the methodology portion of this paper. Each of the nozzle geometries was generated as a series of points which were imported into a CAD program. These geometries were altered such that the De Laval nozzle was set inside of the truncation of the aerospace. This simplified approximation of the compound nozzle was then imported as an STL file into the native CAD programs to the ANSYS suite, Spaceclaim, and design modeler. An image of this geometry for both the initial and final configurations can be seen in figures 26 and 27 respectively below.

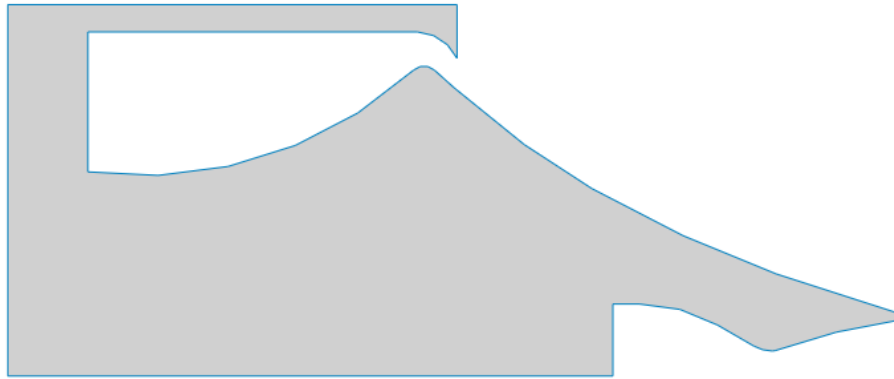


Figure. 6.1: Simplified nozzle geometry for CFD import initial configuration

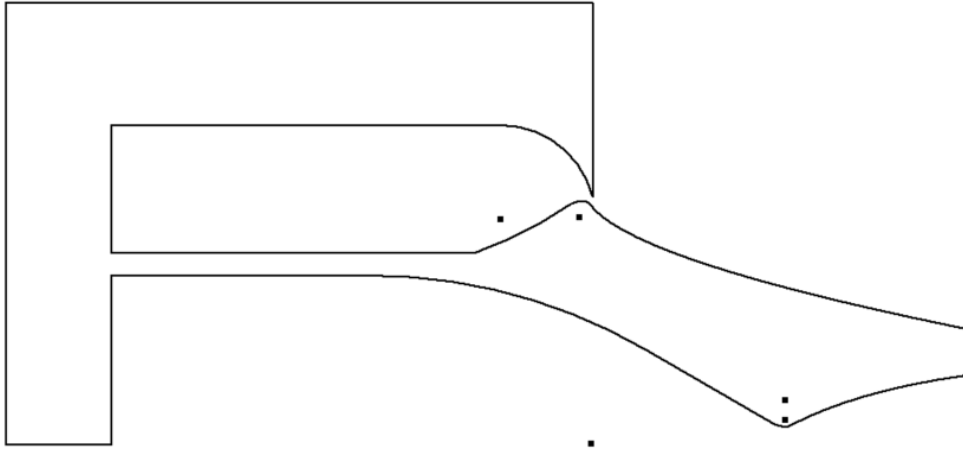


Figure. 6.2: Simplified nozzle geometry for CFD import Final configuration

A structured mesh of largely cartesian configuration with stratified topology was created for the geometry of the compound nozzle and associated flow field. This was accomplished through the overlay of several faces and Boolean removal of the nozzle geometry. The topological construction allowed for the creation of higher density mesh regions in areas of interest, namely each nozzle interior and exit. Stratifying the meshing density in this way allows for reasonably high-fidelity analysis at areas of interest while limiting the computational intensity of each simulation. Illustrations of this mesh configuration for an initial design as well as the finalized design can be seen below in figure 28 and 29. A study was performed on the mesh quality with meshes of varying fidelity to ensure the efficacy of the mesh used as well as the accuracy of the results obtained from its use. Through this process, it was found that the minimum convergence criteria are roughly 45,000 elements.

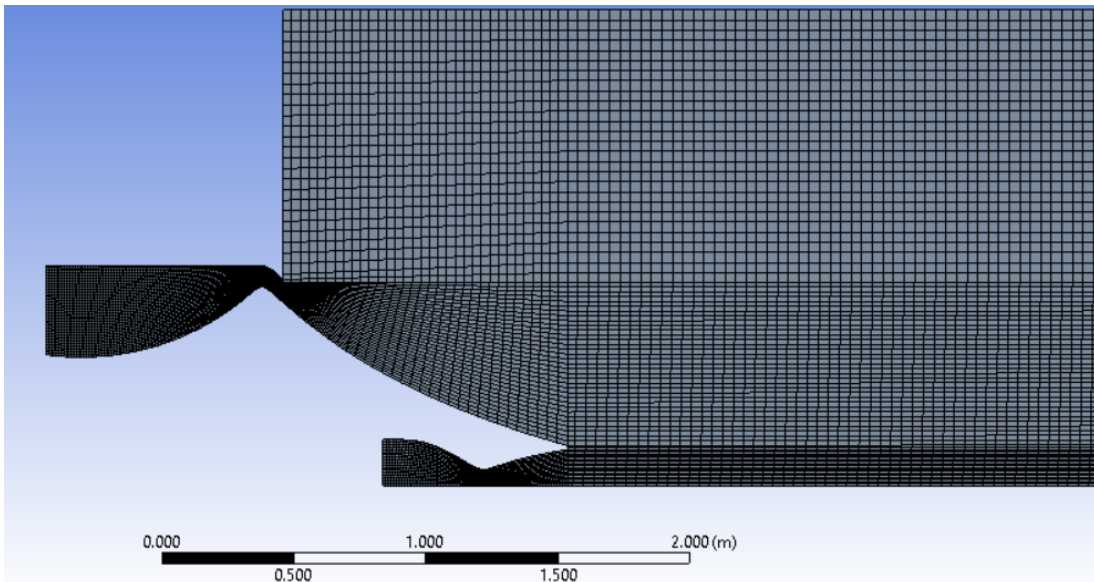


Figure. 6.3: View of fluent meshing topology initial configuration

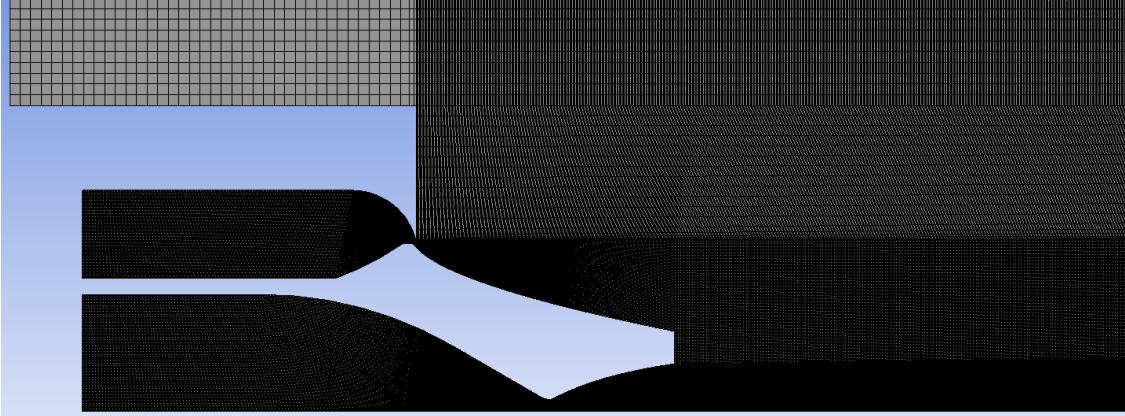


Figure. 6.4: View of fluent meshing topology final configuration

Table 6.1: Compound Nozzle designs: General Settings

General Settings: Compound Nozzle	
Conditions	Settings
General Solver	Density-Based
Simulation State	Steady State
Velocity Formulation	Absolute
Geometric settings	Axisymmetric about the X-axis
Energy equation	On
Viscous Model	K-epsilon RNG (compressibility effects)
Fluid Model	Air (Ideal Gas)

Once the mesh was completed it was subsequently loaded into the Fluid Flow (fluent) plug-in for ANSYS the general settings of each case simulation was set as seen in table 5 above. This is such that the general solver was set to Density-Based. This solves the governing equations of mass momentum and energy concurrently rather than solving sequentially as with the velocity-based model. Additionally with combustion neglected, removing the need for time dependency

the problem was set to steady-state. The geometric settings were set to Axisymmetric about the X-axis such that the 3D geometry of the compound nozzle would be approximated by the 2D.

For the fluid viscosity model, K-Epsilon RNG with compressibility effects was used. This viscous model is a variation on the standard K-epsilon model, however, differs in that it uses a renormalization statistical technique and contains the three refinements. First, it includes an additional term in its epsilon equation that improves solution accuracy. Second, the effect of swirl turbulence is included. The third is the introduction of an analytical formula for turbulent Prandtl numbers. This model was selected for its common use as well as its robustness in relation to compressible fluid flows. The fluid was set to be an ideal gas to account for the high speeds, compressibility, and similarity to the associated ambient conditions [2]

Table 6.2: Compound nozzle designs 1-2: boundary conditions

Boundary Conditions for The Compound Nozzle			
Settings	Inner nozzle Inlet (Pressure)	Outer nozzle Inlet (Pressure)	Outlet (Pressure)
Gauge Pressure	3.0 MPa	3.0-4.6 MPa	60000-101325 Pa
Operating Pressure	0 Pa	0 Pa	0 Pa
Total Temperature	300 K	300 K	300 K
Supersonic gauge pressure	60000-101325 Pa	60000-101325 Pa	N/A
Free Stream Temperature	300 K	300 K	300 K

The boundary conditions for each case were set to reflect the design operating conditions of the engine assembly and changing ambient conditions. For the case of the sea level simulation, the inner nozzle was set to a gauge pressure of 3.0 MPa, and the annular nozzle was set to between 3.0-4.6 MPa (operational range) depending on the run. Both supersonic gauge pressures, as well as the outlet pressure, were set to 1 atm or 101325 Pa. In cases where there is singular nozzle operation the unutilized nozzle inlet was set to be a wall and included in the overall nozzle geometry, thus setting removing the conditions noted in table 6 above.

Following the initial analysis of the first two nozzle configurations, an analysis of the final design was conducted largely utilizing the same process as the aforementioned methodology.

However, in the case of the final configuration, the boundary conditions were altered to suit the changes to the design accordingly. For the case of the sea level simulation, the inner nozzle was set to a gauge pressure of 4.6 MPa, and the annular nozzle was set to between 5-6 MPa (operational range) depending on the run. Both supersonic gauge pressures, as well as the outlet pressure, were set to 1 atm or 101325 Pa. A tabulation of the associated boundary conditions is displayed in table 7 below.

Table 6.3: Compound nozzle Final Design: boundary conditions

Boundary Conditions for final configuration			
Settings	Inner nozzle Inlet (Pressure)	Outer nozzle Inlet (Pressure)	Outlet (Pressure)
Gauge Pressure	4.6 MPa	5-6 MPa	60000-101325 Pa
Operating Pressure	0 Pa	0 Pa	0 Pa
Total Temperature	300 K	300 K	300 K
Supersonic gauge pressure	60000-101325 Pa	60000-101325 Pa	N/A
Free Stream Temperature	300 K	300 K	300 K

Table 6.4: Compound nozzle: solution methods

Solution Methods: Aerospike Case	
Settings	Type
Formulation	Implicit Formulation
Flux type	Roe-FDS
Gradient	Least Squares Cell-Based
Flow	Second-Order Upwind

For the solution methods, second-order settings were used. This was done to provide greater accuracy to each case run. These settings can be seen in table 8 above along with the setting for implicit formulation. Although first-order flow settings would yield better convergence than that of the second-order scheme, the boost in solution accuracy was deemed more beneficial than potential drawbacks.

Standard initialization was used for all iterations such that the initial conditions for each run were manually input. This was coupled with solution steering for supersonic cases for runs at lower ambient pressures. This allows fluent to make some initial assumptions regarding the initialization such that the run does not experience a divergence event early in the process. table 5 below denotes the method, computational reference frame, and the average number of iterations required for a convergent solution.

Table 6.5: Compound nozzle designs 1-2: solution initialization

Solution Initialization: Aerospike Case	
Settings	Type
Initialization Method	Standard Initialization
Computation Reference	From All Zones
Reference Frame	Relative to Cell Zone
Iterations to Convergence	2000

6.1 Single throat operation

Following the design paradigm of the Compound, nozzle to have three operational modes the simulation of both the center and annular nozzle were conducted independently. This allows for the characterization of each nozzle's independent performance and the establishment of each respective mode's operational limits.

6.1.1 De Laval throat operation

For the initial CFD run, it was determined that characterizing the inner de-Laval nozzle would be required first such that its properties could be established as a benchmark and altered accordingly with the simulations of alternate operational modes. Figure 19 below provides the Mach contours of the inner nozzle running at a baseline of 3.0 MPa at 101325 Pa, reflecting the takeoff conditions at earth sea level. The resultant shock diamond formation is typical of a convergent-divergent nozzle under such conditions as the nozzle is shown to be slightly under expanded. The resultant thrust of 49.8 KN meets the expectations of the design under the associated conditions.

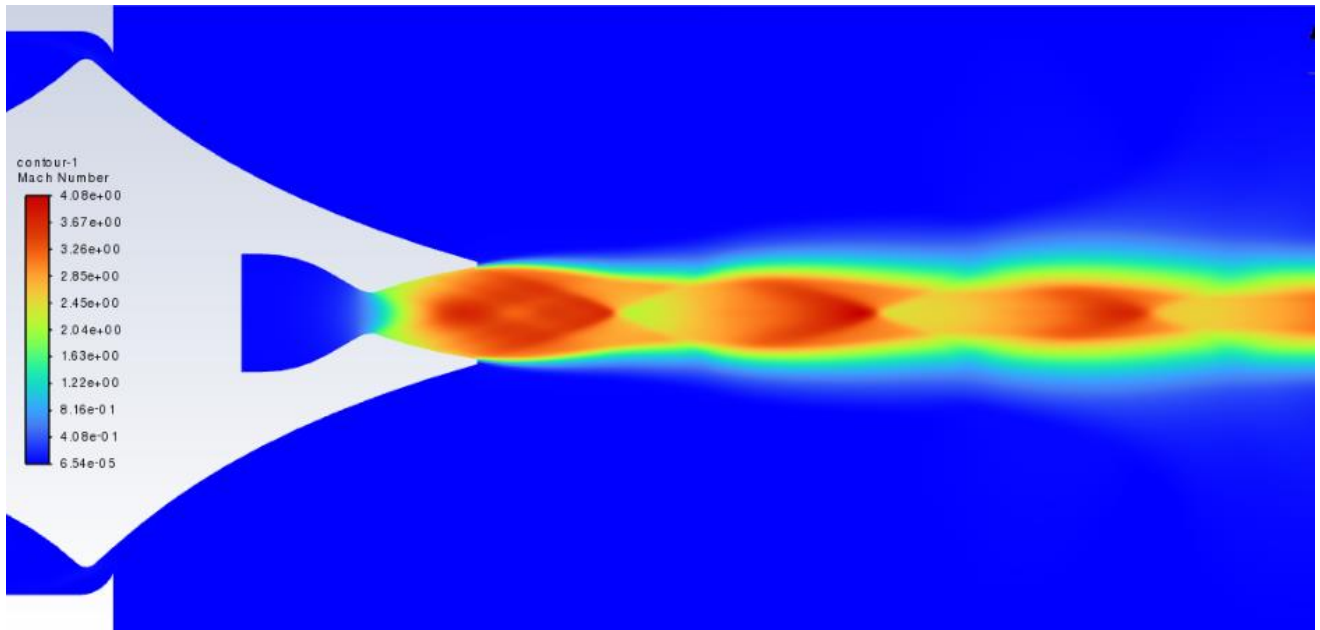


Figure. 6.5: Mach contour of center nozzle operational mode (initial design)

For the final compound nozzle configuration, in a similar fashion to the previous iteration, the characterization of the inner nozzle was accomplished through running at a baseline of 4.6 MPa at 101325 Pa. This resulted in the production of roughly 79 KN of Thrust and like the previous case, the familiar Mach diamond shock wave formation in the wake of the flow is observed. Additionally, detachment of flow is not observed in the solution. A Velocity contour depicting the resultant simulation for the final nozzle configuration is shown in figure 31 below.

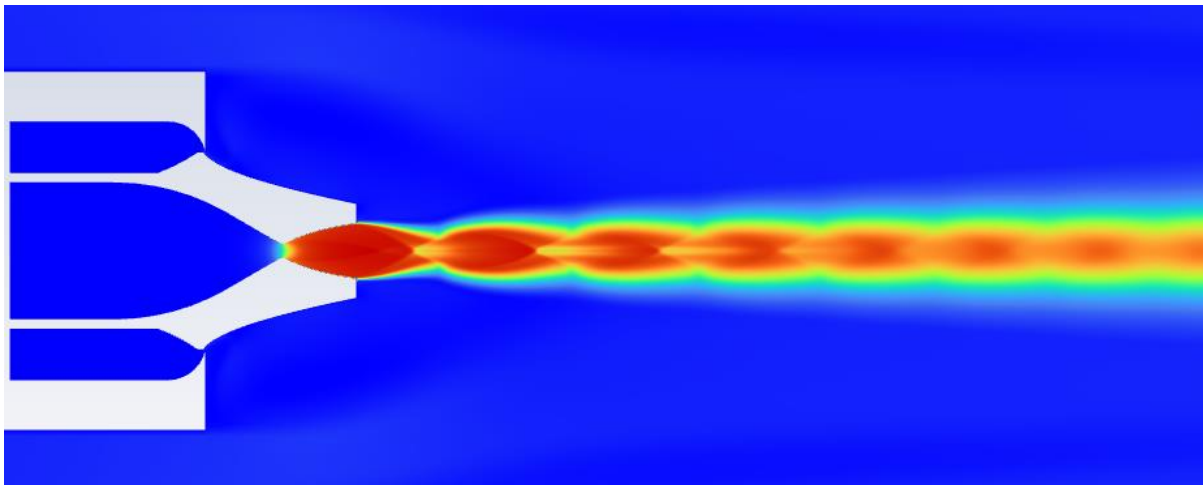


Figure. 6.6: Mach contour of center nozzle operational mode (final design)

6.1.2 Annular throat operation

The second simulation run for the initial designs was that of the annular nozzle in single operation mode. Like that of the center nozzle operational mode, this run took sea-level conditions of 101325 Pa ambient pressure and a nozzle inlet operation pressure of 4.6 MPa. Again, like the previous, this test was undertaken to benchmark the behavior of flow exiting the outer nozzle and observing the resultant. It was a concern that the negative space within the truncation of the spike would result in irregular shock formation or even impingement. Figure 32 below depicts the Mach contour of the nozzle under the aforementioned conditions, and it exhibits the typical characteristic expected of a similar nozzle under the same operational conditions. The formation of the outer jet boundary, envelope shock, and trailing shock can be seen. The flow within the recirculation zone appears to be exacerbated due to the negative space of the inner nozzle, trailing shock, and expansion zone.

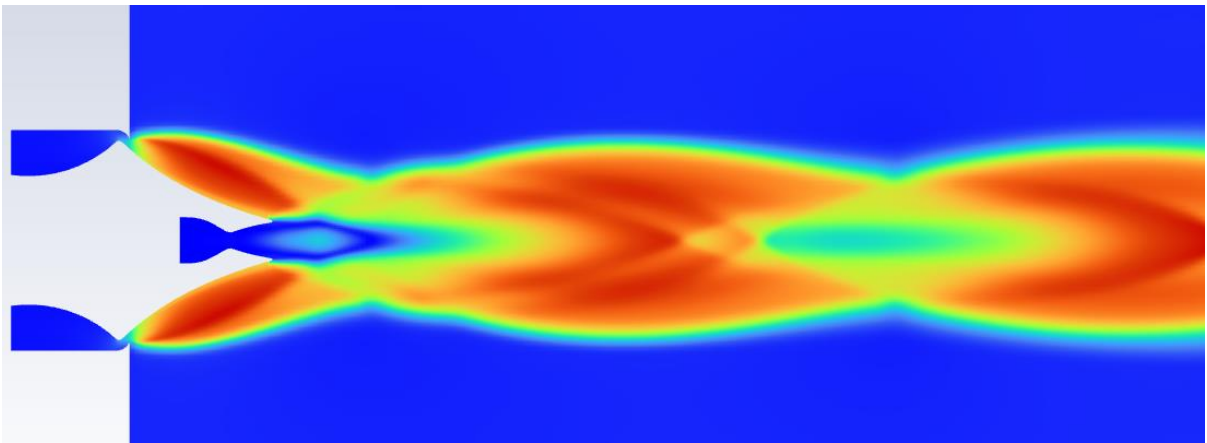


Figure. 6.7: Mach contour of annular nozzle operational mode

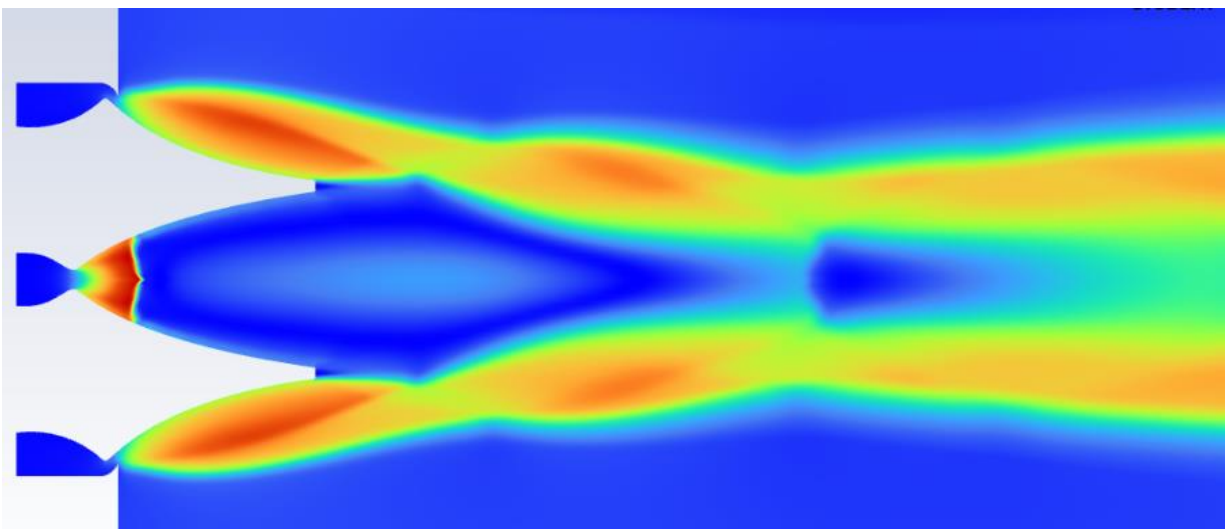


Figure. 6.8: Alternate initial nozzle geometry simulation

The observed conditions from the initial simulations were taken into account for the simulation of the finalized design. Namely, the recirculation zone present in the truncation of aerospike center bodies during the operation was noted to have been exacerbated by the presence of the negative space of the inner nozzle. This resulted in the formation of pressure irregularities corresponding to the size of the nozzle divergent section. Consequently, the final design incorporated a minimal expansion bell. An image of the resulting Mach number contours for a simulation under the same conditions outlined prior is depicted in figure 34 below.

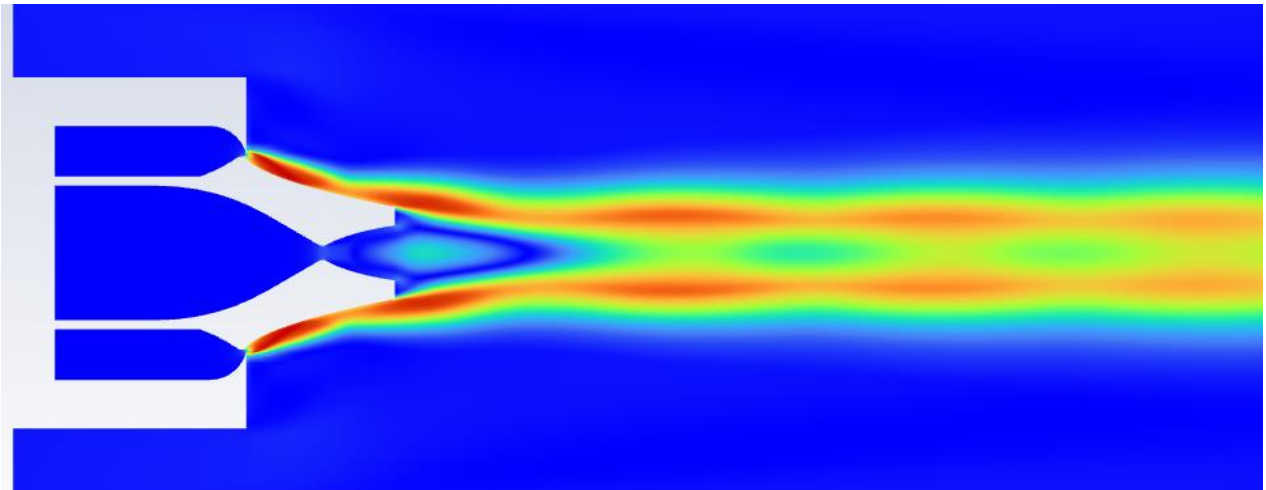


Figure. 6.9: Final nozzle configuration simulation (aerospike)

Performance of the completed design for the annular nozzle saw significant improvement over that of the previous iterations such that the recorded thrust value was 642 KN at a specific impulse of 412s. The accompanying mass flow rate correspondingly rose to a value of 158 Kg/s as well at an exit velocity of Mach 3.98. As a result of this increase in performance the putter annular nozzle represents the bulk of thrust generation of the compound nozzle.

6.2 Dual throat operation

The final series of simulation runs were centered around the dual throat operation mode and were specifically interested in the behavior of each nozzle as they operate simultaneously. The expected result of the simulation at Earth Sea level was that the inner nozzle would behave similarly to that of a nozzle base bleed. Each of the boundary conditions were taken to be the same as the respective run prior however with an additional simulation with the outer nozzle pressure set to 4.6 MPa for the initial iterations and increased to 6 MPa for the final iteration. Interestingly the behavior of the dual-mode was not quite as expected as the normal impingement of shockwaves present in base bleeds was not present indeed for lower annular nozzle pressure the formation of normal socks within the interaction between each nozzle flow was observed. Figure 35 below provides the Mach contours of the dual throat operation mode and showcases these interactions between the shockwaves of each nozzle exhausting flow for an initial iteration and figure 36 below details the same for the final design iteration.

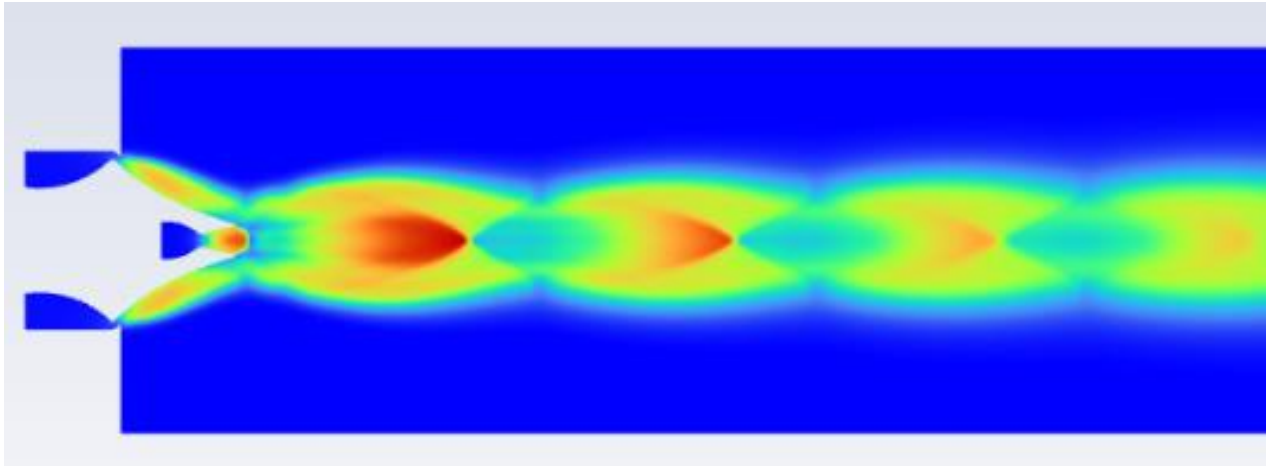


Figure. 6.10: Mach contour of dual nozzle Operational mode

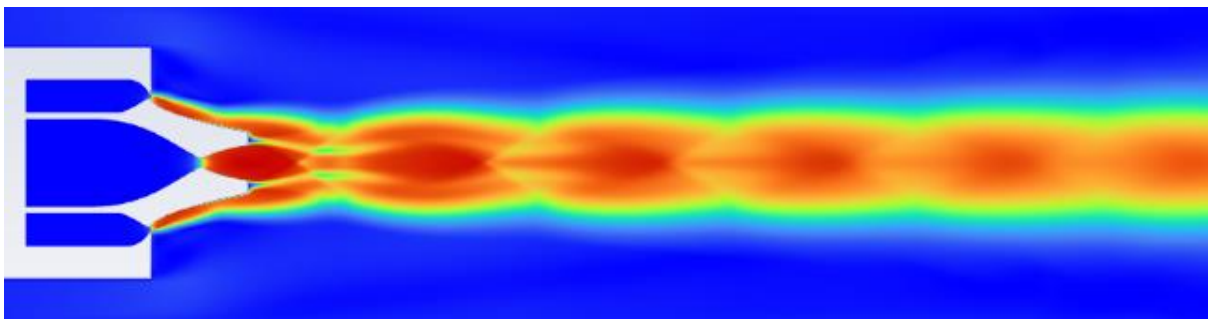


Figure. 6.11: Final compound nozzle configuration run (dual throat)

Following the acquisition of the data from each of the aerospike simulations, calculations were performed to corroborate the information obtained. Taking into account the properties of the propellants and the associated combustion and utilizing equation 3.10 the exit velocity of the propellants was obtained relative to the gas properties. Following this, the calculation of the equivalent velocity was obtained through equation 3.7. Taking into account the total mass flow rate of 21.19 kg/s, the pressure conditions, and the exit area of the spike and the inner nozzle, the equivalent velocity was determined for the baseline atmospheric case. The equivalent velocity was determined to be 3861.4 m/s for the simultaneously firing of both the inner and outer nozzle. With these values in hand, utilizing equation 6.1 below the sea-level specific impulse of the inner engine was determined to be 394s. correspondingly the vacuum specific impulse is expected to be a larger value.

$$I_{sp} = \frac{V_{eq}}{g_0}$$

6.1

Taking into account the performance values of both the inner and outer nozzle the following table was generated to record the operational characteristics of the compound nozzle under sea level conditions.

Table 6.6: Compound nozzle performance breakdown

Compound Nozzle performance characterization		
Metric	Annular nozzle	De-laval nozzle
Thrust	642.12 KN	82.03 KN
Specific Impulse	412.7s	394.75s
Total mass flow rate	158kg/s	21.19kg/s

6.3 Altitude study

In order to fully discern the behavior of the compound nozzle under dual throat operation, an altitude study was performed such that each simulation of the modes previously discussed was rerun under increasingly lower pressure ambient conditions to simulate the rising through either Earth or Martian atmosphere. The behavior of the center nozzle was of particular note with these simulation runs as under normal circumstances it would become increasingly over-expanded. Engine performance was observed to determine what effects if any were imposed by the delta in ambient conditions. Figure 38 shows the Mach contours of one such simulation run at an ambient pressure of 50,000 Pa with the same dual-mode operating conditions outlined in the previous section for the initial configuration.

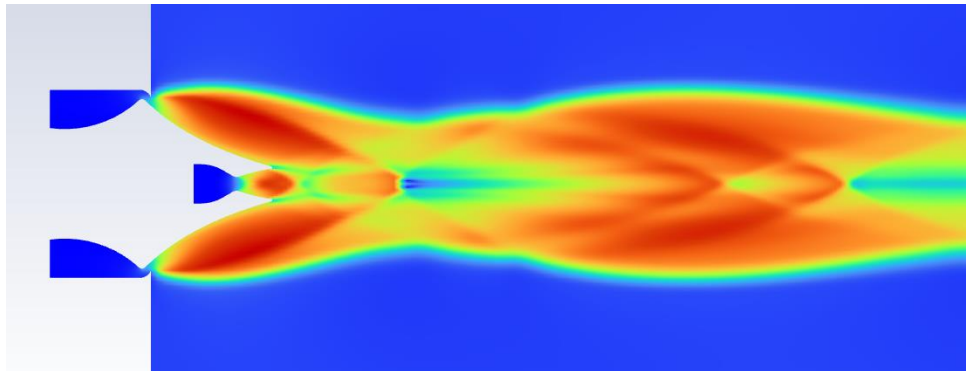


Figure. 6.12: Mach contour of dual nozzle operational mode 50,000 Pa

Figure 37 below depicts the single-mode operation of the aerospike under the ambient conditions discussed in the previous case. These simulations were conducted under each of the operational mode profiles.

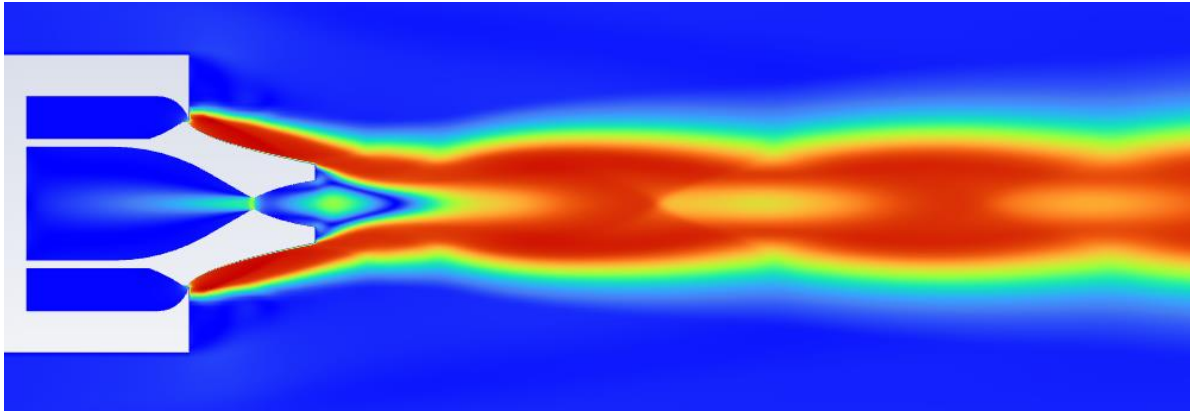


Figure. 1.9: Velocity contour of outer nozzle operational mode 50,000 Pa

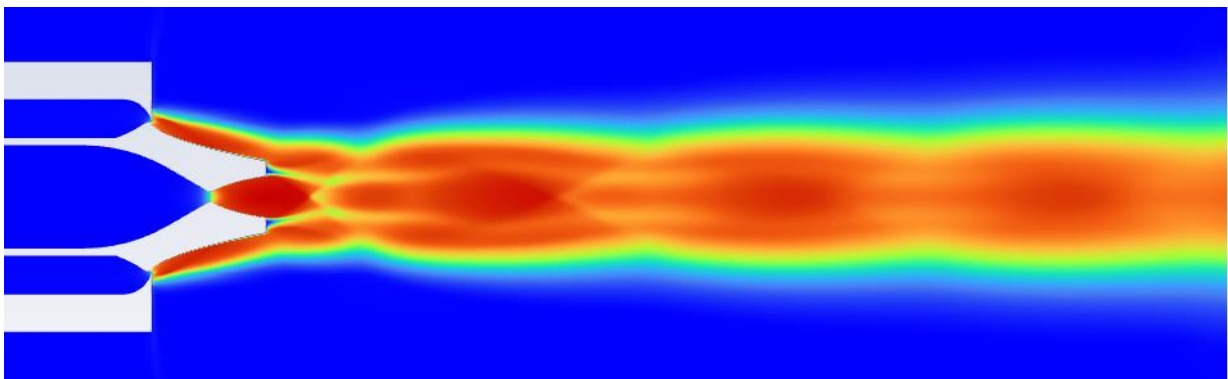


Figure. 6.13: Velocity contour of dual nozzle operational mode 50,000 Pa

It is noted that the expected behavior of the system is such that the outer aerospike nozzle represents the driving element behind the expansion conditions of the inner nozzle, initial simulations show that the expected behavior is present. However, this is such that the results were not as expected, while the inner nozzle does see greater expansion with the annular nozzle exhaust acting as an envelope for the flow, there is a pervasive presence of a normal shock in the interior nozzle and flow along the exhaust path of the inner nozzle.

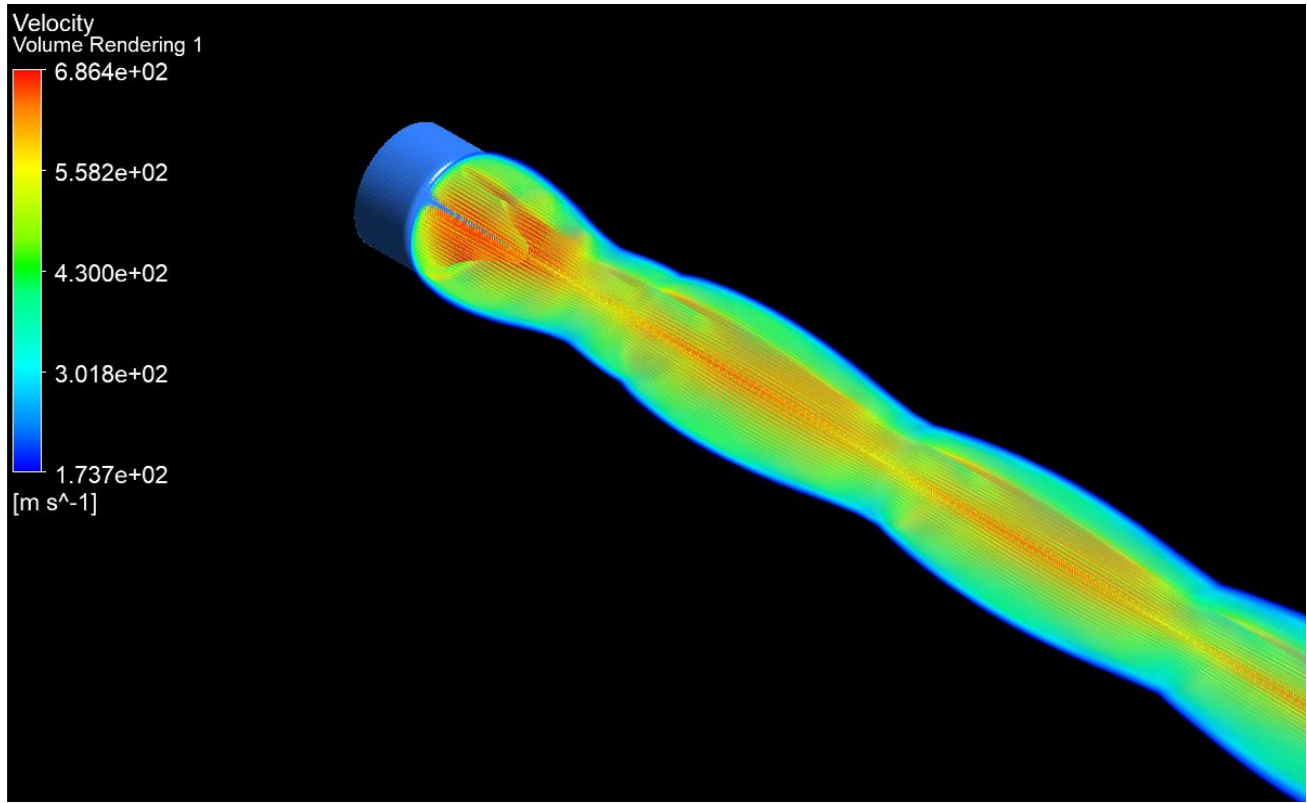


Figure. 6.14: 3D nozzle flow representation (dual mode)

7. Discussion

The objective of this investigation was the coupling of a convergent-divergent nozzle and a truncated toroidal aerospike nozzle into a dual throat nozzle. The desired outcome of the coupling of these systems was to take advantage of the passively altitude compensating properties inherent in the aerospike design and mitigate the losses of the inner nozzle associated with the expansion properties inherent to traditional designs. The results obtained through the computational fluid dynamics simulations reveal that this expected behavior is not necessarily accurate as the results deviate from these expectations slightly.

Specifically, it was observed that the recirculation zone located at the base of the truncation had a much larger effect on the behavior of the inner nozzle than expected. In the initial design iterations this resulted in the consistent formation of normal shocks within the inner nozzle regardless of ambient pressure conditions. Consequently, this required a redesign of the inner nozzle from those of more low pressure ambient condition design to that of higher pressure/ sea level expansion ratios. Additionally, it was noted that in order to compensate for this shock formation in the dual operational mode the chamber pressure of the inner nozzle needed to exceed that of the chamber pressure of the annular nozzle. Should it have been the other way around or the chamber pressures have been equal, normal shock formation at some point along the divergent portion of the inner nozzle was observed largely independent of exterior expansion conditions down to 30,000 pa. It was however noted that the exterior flow of the annular nozzle did envelop the interior flow of the convergent divergent nozzle such that it was able to operate at similar expansion conditions at much larger ranges than would otherwise occur.

With the resolution level at which the system analysis was conducted, it was found that the compound nozzle would be able to provide the necessary performance for its intended mission profile. Additionally, the incorporation of a dual expander cycle to cool the inner and outer nozzles independently was verified to be a viable cycle for such a configuration. The cooling of such a system would otherwise represent a significant complication in the design. However, upon the utilization of the computational analysis results and subsequent calculations it was determined that the gains over a similarly sized system of either an aerospike or de Laval nozzle would perform similarly. The gains seen in thrust and specific impulse for the system are observed to be limited.

8. Future Development

For continued development in the future, there are two areas that require further investigation. Namely greater stipulation on the design of the dual expander cycle along with the accompanying turbomachinery and valves would be necessary. The current documentation accounts for the systems-level design of these systems however the detailed technical designs would add allow for greater fidelity of the performance analysis of the nozzle design. Additionally, the development of appropriate propellant injection for each of the nozzles incorporated into the compound configuration, as well as an instability analysis that results from the concentric design would be required prior to any endeavors into practical testing of the novel configuration. Specifically, the identification of the injection type i.e. pintle, plate, like doublet, unlike triplite, etc. Lastly greater fidelity of the CFD simulation with higher power processing would not only increase simulation accuracy but analysis time associated with simulation results.

9. Conclusions

Upon review of the CFD analysis performed in this paper along with the associated system's design. It was determined that the compound nozzle in conjunction with a dual expander cycle has the potential to provide greater variability in a single system while simultaneously extending its life cycle. Gains in both fuel consumption and specific impulse were attained however due to the complexity of the accompanying systems and the associated increase in weight the engine only performs slightly better than that of contemporary engines. Additionally, with the pervasive presence of normal shock formation in the inner flow during dual operation mode and the increased magnitude of the recirculation zone at the base of the aerospike center body truncation, the design aspects of the compound nozzle prove to be difficult and potentially inefficient if not carefully designed such that these factors are not a hindrance. That being said, it can be concluded that the outer annular nozzle performed as expected and compensated for the poor expansion properties of the inner convergent-divergent nozzle such that its application as a Mars sample return vehicle is viable, though additional development of the accompanying systems and nozzle geometry is required.

Acknowledgments

I would like to express our great appreciation to Dr. Papadopoulos for his valuable assistance through the development of this project. His willingness to give his time and knowledge so generously has been very much appreciated. Additionally, would like to express my gratitude to my college Kyle Stewart for his aid in the development of the aerospike geometry as well as collaborations we have conducted on similar research. Lastly, I would like to express my gratitude to the aerospace engineering department at San Jose State University for facilitating my work and providing a fantastic foundation of knowledge and a wonderful community during the duration of my education.

References

- [1] Hagemann, G., Immich, H., Van Nguyen, T., and Dumnov, G. E., “Advanced rocket nozzles,” *Journal of Propulsion and Power*, vol. 14, 1998, pp. 620–634.
- [2] Stewart, K. J., Papadopoulos, P., and Pollard, J., “Nuclear thermal rocket engine with a toroidal aerospike nozzle,” *AIAA Propulsion and Energy 2020 Forum*, 2020.
- [3] Sequeira, C. W., and Sanjay, M. V., “Efficiency analysis of aerospike nozzle by comparison with a de-Laval nozzle using computational fluid dynamics,” *Lecture Notes in Mechanical Engineering*, 2021, pp. 467–476.
- [4] Ito, T., and Fujii, K., “Flow field and performance analysis of an annular-type aerospike nozzle with base bleeding,” *TRANSACTIONS OF THE JAPAN SOCIETY FOR AERONAUTICAL AND SPACE SCIENCES*, vol. 46, 2003, pp. 17–23.
- [5] Ito, T., and Fujii, K., “Numerical investigations of the base-flow characteristics of axisymmetric aerospike nozzles,” *TRANSACTIONS OF THE JAPAN SOCIETY FOR AERONAUTICAL AND SPACE SCIENCES*, vol. 45, 2002, pp. 108–115.
- [6] Angelino G., “Approximation Method for Plug Nozzle Design”, *AIAA Journal*, Vol. 2, No. 10, Oct.1964, pp. 1834-1835.
- [7] Nair, P. P., Suryan, A., and Kim, H. D., “Computational study on flow through truncated conical plug nozzle with base bleed,” *Propulsion and Power Research*, vol. 8, 2019, pp. 108–120.
- [8] Shenoy, A. R., Sreekumar, T. S., Menon, P., and Alex, G., “Computational Analysis of Dual Expander Aerospike nozzle,” *Advances in Mechanical Engineering*, 2020, pp. 151–158.
- [9] Johnson G.R., Doyle Thompson H. and Hoffman J.D (1974), ‘Design of maximum thrust plug nozzles with variable inlet geometry’, *Computers and Fluids*, Vol 2, pp 173-190.
- [10] Lee, C. C., “Computation of plug nozzle contours by the Rao’s optimum thrust method”, *NASA CR-21914 R-61*, 1963.
- [11] Masuda, R., “Optimal design of annular aerospike engine nozzle,” thesis, ProQuest Information and Learning Company, 2003.
- [12] Eilers S.D., Matthew D., Wilson and Whitmore S.A. (2010), ‘Analytical and experimental evaluation of aerodynamic thrust vectoring on an aerospike nozzle’, *Joint Propulsion & International Energy Conversion Engineering Conferences*, AIAA-jpc-10.
- [13] Mattingly J. D., *Elements of Propulsion : Gas Turbines and Rockets*. Reston, Virginia: American Institute of Aeronautics and Astronautics, 2012.
- [14] McVay, E. S., “Design of a dual-expander aerospike nozzle rocket engine,” thesis, University of Alabama Libraries, 2016.
- [15] Li J., Liu Y., Liao Y and Wang C (2010), ‘Experimental and numerical study on two dimensional plug nozzle’, *46th AIAA/ASME/SAE/ASEE Joint Propulsion Conference & Exhibit*, AIAA paper 2010-6659, 2010.

- [16] Naveen. Kumar, & Antony Daniel. "Design and Optimization of Aerospike nozzle using CFD". Retrieved https://www.bing.com/cr?IG=57C6097D888D4884B9E65FC13D7B5AFD&CID=0DEA23F771E16F1B0AB32805704E6EE0&rd=1&h=X11yLte9JOWmoQThMkUINeARPz9yBH8rH0fhuP5ptDM&v=1&r=https://www.researchgate.net/publication/320438795_Design_and_Optimization_of_Aerospike_nozzle_using_CFD&p=DevEx.LB.1, 5488.1
- [17] Paul V. Tartabini, Roger A. Lepsch, Korte, J. J., and Kathryn E. Wurster, 2000, "A Multidisciplinary Performance Analysis of A Lifting-Body Single-Stage-to-Orbit Vehicle", AIAA-2000-1045. Trans. Roy. Soc. London, vol. A247, pp. 529-551, April 1955.
- [18] Shannon D. Eilers, Matthew D. Wilson, and Stephen A. Whitmore, 2010, "Analytical and Experimental Evaluation of Aerodynamic Thrust Vectoring on an Aerospike Nozzle", 46th AIAA/ASME/SAE/ASEE Joint Propulsion Conf. & Exhibit, Nashville, TN.
- [19] Takeo T., Nobuhiko K. and Akira O. (2010), 'A conceptual system design study for a linear aerospike engine applied to a future SSTO vehicle', 46th AIAA/ASME/SAE/ASEE Joint Propulsion Conference & Exhibit, AIAA paper 2010-7060, 2010.
- [20] Verma, S. B., 2009, "Study of Restricted Shock Separation Phenomenon in a Thrust Optimized Parabolic Nozzle", J. Propulsion and Power.
- [21] Wang, Y., Xu, J., Huang, S., Lin, Y., and Jiang, J., "Computational study of axisymmetric divergent bypass dual throat nozzle," *Aerospace Science and Technology*, vol. 86, 2019, pp. 177–190.

Appendix A- Simple Ideal Rocket Theory Calculation Code

```

clear all;
close all;
%% Theoretical Performance Parameters
Pc = 2.4e6; % chamber pressure Pascals
At = 0.01482;% M^2
OF = 4.5; % oxidizer to fuel ratio
ER = 280; % expansion ration Ae/At
Pe = 100000; % Pascals nozzle exit pressure
Pa = 101325; % Pascals ambient pressure
Ra= 8314; % universal gas constant J/K*Mol
g= 9.8; % m/s^2
y= 1.2247; % specific heat ratio
Ti= 300; % initial temp kelvin
Hv = 142000; % heating value of H KJ/kg
Cp = 3.4; % specific heat at constant pressure
Mw = 18.02; % Molecular mass of combustion g/mol
Ae = At*ER; % exit area m^2

% for OF = 2:0.25:20 % oxidizer to fuel ratio
L= sqrt((y*((1+y)/2)^((1+y)/(1-y)))) % Vandekerckhove function

%fprintf('Chamber Temperature k')
Tc = Ti+((Hv)/(Cp*(1+OF))) % Chamber temperature

%fprintf('Mass Flow Rate kg/s')
mdot = ((Pc*At)/(sqrt((Ra/Mw)*Tc)))*L % mass flow rate

%fprintf('Nozzle Exit Velocity m/s')
Ve= sqrt(((2*y)/(y-1))*(Ra/Mw)*Tc*(1-(Pe/Pc)^((y-1)/y))) % exit velocity

%fprintf('Engine Thrust KN')
F_t= (mdot*Ve+(Pe-Pa)*Ae)/1000 % Thrust equation

%fprintf('Specific Impulse S')
ISP= Ve/g % Specific Impulse

figure(1)
plot(Tc,ISP,'k--')
xlabel('Chamber Temperature K');
ylabel('Specific Impulse S');
title({'ISP VS TC'});

```

```
figure(2)
plot(OF,ISP,'k--')
xlabel('Oxidizer to Fuel Ratio');
ylabel('Specific Impulse S');
title({'ISP VS OF'});
```

```
figure(3)
plot(Tc,OF,'k--')
xlabel('Chamber Temperature K');
ylabel('Oxidizer to Fuel Ratio');
title({'TC VS OF'});
```

```
hold on
end
```

,

Appendix B- Orbit Transfer Trajectory Code

```

clear all;
close all;
clc;
%-----
% constants
hours=5800;
G=6.6742e-20;           % gravitational values
M_Sun=1.989e30;        % mass of Sun
% R_Sun=695800;        % radius of Sun in Km
% R_Earth=6378;        % radius of earth in Km
% R_Mars=3397;         % radius of mars in Km
R_Sun=7958000;         % radius of Sun in Km (not to scale)
R_Earth=5378000;       % radius of earth in Km (not to scale)
R_Mars=4397000;        % radius of mars in Km (not to scale)
r0E= [-0.0433e8 1.4703e8 0.0000];
v0E=[-30.2688 -0.8912 0.0000];
r0M= [1.8630e8 0.8938e8 -0.0271e8];
v0M=[-11.4466 23.8820 0.7819];
r0T=[-0.0433e8 1.4703e8 0.0000]; % intial position in km Earth orbit
% r0T=[149967000 -293159 0]; % intial position in km Earth orbit
v0T=[-33.6661 -0.9913 0.0000]; % initial Velocity in km/s Earth orbit
r03=[-1.1334e8 2.3919e8 0]; % intial position in km Mars Orbit
v03=[-23.6322 -9.6601 0]; % initial Velocity in km/s Mars Orbit
%Hyperbolic Trajectory:

t0=0; % intial time
tf=95000000; % intial time transfer
t0M=0; % intial time
tfM=98400000;
t0T=0; % intial time
tfT=200000000;
t03=200000000; % intial time transfer
tf3=300002800; % time of flight/final time transfer
theta=0:0.01:2*pi;
y0=[r0E v0E]';
y0M=[r0M v0M]';
y0T=[r0T v0T]';
y03=[r03 v03]';
%-----
% ODE45 construction
options = odeset('RelTol',1e-10,'AbsTol',1e-10);
[tE,fe]=ode45(@ratesSun,[t0 tf],y0,options);

```

```

[tM,fM]=ode45(@MarsorbitSun,[t0M tfM],y0M,options);
[fT,fT]=ode45(@EarthMarsTransfer,[t0T tfT],y0T,options);
% [t3,f3]=ode45(@rates2,[t03 tf3],y03,options);
% -----
%Plot of 3D Orbit
xout=fE(:,1);
yout=fE(:,2);
zout=fE(:,3);
xoutM=fM(:,1);
youtM=fM(:,2);
zoutM=fM(:,3);
xoutT=fT(:,1);
youtT=fT(:,2);
zoutT=fT(:,3);
[XM,YM,ZM] = sphere;
XM=XM*R_Mars;
YM=YM*R_Mars;
ZM=ZM*R_Mars;
[XE,YE,ZE] = sphere;
XE=XE*R_Earth;
YE=YE*R_Earth;
ZE=ZE*R_Earth;
[X,Y,Z] = sphere;
X=X*R_Sun;
Y=Y*R_Sun;
Z=Z*R_Sun;
fig=figure();
set(fig,'color','white')
plot3(xout, yout, zout,'b-',xoutM, youtM, zoutM,'r-',xoutT, youtT, zoutT,'g-', 'linewidth',4)
% plot3(xoutM, youtM, zoutM,'r-', 'linewidth',4)
% plot3(xoutT, youtT, zoutT,'g-', 'linewidth',4)
grid on
hold on
axis equal
surf(X,Y,Z,'FaceColor','y','FaceAlpha',.5)
surf(XM-64963100,YM-231581000,ZM-3253790,'FaceColor','r','FaceAlpha',.5)
surf(XE+1842520,YE+147084000,ZE,'FaceColor','b','FaceAlpha',.5)
title('Mission Profile: Sun Center Transfer');
xlabel('x km');
ylabel('y km');
zlabel('z km');
legend('Earth Orbit','Mars Orbit','Transfer Orbit');
% -----
% Animation
figure;
hold all;

```

```

[Sun_x,Sun_y,Sun_z] = sphere;
surf(Sun_x*R_Sun,Sun_y*R_Sun,Sun_z*R_Sun,'FaceColor','y','FaceAlpha',.5);
myLines(1) = plot3(NaN, NaN, NaN,'LineWidth',1);
myLines(2) = plot3(NaN, NaN, NaN, '-b','LineWidth',1);
myLines(3) = plot3(NaN, NaN, NaN,'LineWidth',1);
myLines(4) = plot3(NaN, NaN, NaN, '-r','LineWidth',1);
myLines(5) = plot3(NaN, NaN, NaN,'LineWidth',1);
myLines(6) = plot3(NaN, NaN, NaN, '-g','LineWidth',1);
n_time_faster = 1500;
time_pause = 30/n_time_faster;
np = 10;
title('Mission Profile: Sun Center Transfer');
xlabel('x km');
ylabel('y km');
zlabel('z km');
grid on;
axis equal;
view(45, 10);
rotate3d on;
tam=length(tE);
tamM = length(fM);

% Earth orbit animaition
for k = 1:np:tam
    pause(time_pause);
    set(myLines(1), 'XData', fE(1:k-1,1), 'YData', fE(1:k-1,2), 'ZData', fE(1:k-1,3));
    set(myLines(2), 'Marker','o','color','b','XData', fE(k,1), 'YData', fE(k,2), 'ZData',
fE(k,3));
    drawnow;
end
% Mars orbit animation
for kM = 1:np:tamM
    pause(time_pause);
    set(myLines(3), 'XData', fM(1:kM,1), 'YData', fM(1:kM,2), 'ZData', fM(1:kM,3));
    set(myLines(4), 'Marker','o','color','r','XData', fM(kM,1), 'YData', fM(kM,2), 'ZData',
fM(kM,3));
    drawnow;
end
myLines(1) = plot3(NaN, NaN, NaN,'LineWidth',1);
tamT = length(fT);
% Perform the plotting for transfer
for kT = 1:np:tamT
    pause(time_pause);
    set(myLines(5), 'XData', fT(1:kT,1), 'YData', fT(1:kT,2), 'ZData', fT(1:kT,3));
    set(myLines(6), 'Marker','^','color','g','XData', fT(kT,1), 'YData', fT(kT,2), 'ZData',
fT(kT,3));

```

```

    drawnow;
end
% myLines(5) = plot3(NaN, NaN, NaN,'LineWidth',1);
% myLines(6) = plot3(NaN, NaN, NaN, '-b','LineWidth',1);
% tam3 = length(f3);
% % Perform the plotting for transfer
% for k3 = 1:np:tam3
%     pause(time_pause);
%     set(myLines(5), 'XData', f3(1:k3,1)-64963100, 'YData', f3(1:k3,2)-231581000,
'ZData', f3(1:k3,3)-3253790);
%     set(myLines(6), 'Marker','o','XData', f3(k3,1)-64963100, 'YData', f3(k3,2)-
231581000, 'ZData', f3(k3,3)-3253790);
%     drawnow;
% end
%-----
% state space function construction
function dydt = ratesSun(tE,fE)
G=6.6742e-20;          % gravatiational values
M_Sun=1.989e30;       % mass of Earth
mu=G*(M_Sun);
x=fE(1);
y=fE(2);
z=fE(3);
vx=fE(4);
vy=fE(5);
vz=fE(6);
r=norm([x y z]);
ax=-mu*x/r^3;
ay=-mu*y/r^3;
az=-mu*z/r^3;
dydt=[vx vy vz ax ay az ]';
end

function dfdt = MarsorbitSun(tM,fM)
G=6.6742e-20;          % gravatiational values
M_Sun=1.989e30;       % mass of The Sun
mu=G*(M_Sun);
xM=fM(1);
yM=fM(2);
zM=fM(3);
vxM=fM(4);
vyM=fM(5);
vzM=fM(6);
rM=sqrt(xM^2+yM^2+zM^2);
axM=-mu*xM/rM^3;

```

```

ayM=-mu*yM/rM^3;
azM=-mu*zM/rM^3;
dfdt=[vxM vyM vzM axM ayM azM ]';
end

```

```

function dfdt = orbitchange(t2,f2)
G=6.6742e-20;          % gravatiational values
M_Earth=5.974e24;     % mass of Earth
mu=G*(M_Earth);
% G=6.6742e-20;      % gravatiational values
% M_Mars=0.64169e24; % mass of mars
% mu=G*(M_Mars);
x2=f2(1);
y2=f2(2);
z2=f2(3);
vx2=f2(4);
vy2=f2(5);
vz2=f2(6);
r2=sqrt(x2^2+y2^2+z2^2);
ax2=-mu*x2/r2^3;
ay2=-mu*y2/r2^3;
az2=-mu*z2/r2^3;
dfdt=[vx2 vy2 vz2 ax2 ay2 az2 ]';
end

```

Appendix C- Inner Nozzle Contour

x,mm	r, mm		
#-----		1633.957	65.12934
		1635.443	64.55272
0	562.8885	1636.939	64.00302
277.7726	562.8885	1638.445	63.48043
310.9367	562.5891	1639.96	62.98511
344.0899	561.691	1641.484	62.51722
377.2215	560.1945	1643.016	62.07692
410.3207	558.1001	1644.556	61.66436
443.3766	555.4084	1646.103	61.27966
476.3786	552.1204	1647.656	60.92295
509.3159	548.2371	1649.216	60.59434
542.1777	543.7598	1650.782	60.29396
574.9533	538.6899	1652.352	60.02188
607.632	533.0291	1653.928	59.77821
640.2031	526.7792	1655.507	59.56301
672.6562	519.9423	1657.09	59.37637
704.9805	512.5206	1658.676	59.21833
737.1656	504.5166	1660.265	59.08896
769.2009	495.9328	1661.856	58.9883
801.076	486.7719	1663.448	58.91637
832.7805	477.0372	1665.042	58.87321
864.3041	466.7316	1666.636	58.85882
895.6365	455.8585	1667.444	58.87334
926.7675	444.4215	1667.847	58.89148
957.6869	432.4244	1668.25	58.91687
988.3847	419.871	1668.653	58.9495
1018.851	406.7654	1669.055	58.98936
1049.075	393.1119	1669.456	59.03644
1079.049	378.915	1669.857	59.09072
1108.761	364.1792	1670.256	59.15219
1138.202	348.9094	1670.654	59.22082
1167.362	333.1106	1671.051	59.29659
1196.233	316.7879	1671.446	59.37949
1622.492	70.6872	1671.84	59.46947
1623.879	69.90267	1672.232	59.56651
1625.281	69.14333	1672.623	59.67059
1626.696	68.40942	1673.011	59.78166
1628.124	67.70117	1673.398	59.8997
1629.564	67.01882	1673.782	60.02465
1631.017	66.36259	1674.164	60.1565
1632.481	65.73269	1674.543	60.29518

1674.92	60.44065	1833.807	111.9694
1678.451	61.83355	1837.337	112.8803
1681.982	63.21415	1840.868	113.782
1685.512	64.58254	1844.399	114.6747
1689.043	65.93878	1847.93	115.5582
1692.574	67.28242	1851.461	116.4328
1696.105	68.6141	1854.991	117.2984
1699.636	69.93391	1858.522	118.155
1703.167	71.24192	1862.053	119.0029
1706.697	72.53786	1865.584	119.8419
1710.228	73.822	1869.115	120.6722
1713.759	75.09459	1872.645	121.4937
1717.29	76.3557	1876.176	122.3067
1720.821	77.60541	1879.707	123.111
1724.351	78.84343	1883.238	123.9068
1727.882	80.07011	1886.769	124.6941
1731.413	81.28562	1890.299	125.473
1734.944	82.49004	1893.83	126.2434
1738.475	83.68343	1897.361	127.0055
1742.005	84.86579	1900.892	127.7594
1745.536	86.03696	1904.423	128.5049
1749.067	87.19733	1907.954	129.2423
1752.598	88.34695	1911.484	129.9715
1756.129	89.48591	1915.015	130.6926
1759.659	90.61427	1918.546	131.4057
1763.19	91.7321	1922.077	132.1107
1766.721	92.83935	1925.608	132.8077
1770.252	93.93601	1929.138	133.4969
1773.783	95.02235	1932.669	134.1781
1777.314	96.09843	1936.2	134.8516
1780.844	97.16431	1939.731	135.5172
1784.375	98.22006	1943.262	136.1751
1787.906	99.26574	1946.792	136.8253
1791.437	100.3014	1950.323	137.4678
1794.968	101.3271	1953.854	138.1025
1798.498	102.3429	1957.385	138.7297
1802.029	103.3488	1960.916	139.3493
1805.56	104.3448	1964.446	139.9615
1809.091	105.3312	1967.977	140.5662
1812.622	106.308	1971.508	141.1635
1816.152	107.2751	1975.039	141.7534
1819.683	108.2328	1978.57	142.336
1823.214	109.181	1982.101	142.9113
1826.745	110.1198	1985.631	143.4793
1830.276	111.0492	1989.162	144.04

1992.693 144.5934
1996.224 145.1398
1999.755 145.679
2003.285 146.2112
2006.816 146.7364

2010.347 147.2546
2013.878 147.7657
2017.409 148.2698
2019.717 148.5958

Appendix D- Aerospike Contour

X, m	Y,m		
-0.03495	0.773612	-0.00524	0.766087
-0.02501	0.773583	-0.005	0.765787
-0.02212	0.773529	-0.00475	0.765483
-0.02023	0.773459	-0.0045	0.765173
-0.01881	0.773375	-0.00425	0.764859
-0.01767	0.773279	-0.004	0.764541
-0.01672	0.773173	-0.00374	0.764218
-0.0159	0.773057	-0.00348	0.76389
-0.01519	0.772932	-0.00322	0.763557
-0.01455	0.772799	-0.00296	0.763219
-0.01398	0.772658	-0.00269	0.762877
-0.01346	0.77251	-0.00242	0.76253
-0.01298	0.772355	-0.00214	0.762178
-0.01254	0.772193	-0.00186	0.761821
-0.01213	0.772024	-0.00158	0.761459
-0.01174	0.77185	-0.00129	0.761093
-0.01137	0.771669	-0.001	0.760721
-0.01103	0.771483	-0.0007	0.760344
-0.01069	0.77129	-0.00039	0.759963
-0.01038	0.771093	-8.55E-	
-0.01007	0.770889	05	0.759576
-0.00978	0.770681	0.000228	0.759184
-0.00949	0.770467	0.000547	0.758787
-0.00921	0.770248	0.000872	0.758385
-0.00894	0.770024	0.001203	0.757978
-0.00868	0.769795	0.00154	0.757565
-0.00842	0.769561	0.001883	0.757147
-0.00817	0.769322	0.002232	0.756724
-0.00791	0.769079	0.002588	0.756295
-0.00767	0.76883	0.002951	0.755861
-0.00742	0.768577	0.003321	0.755422
-0.00718	0.768319	0.003698	0.754977
-0.00693	0.768056	0.004082	0.754526
-0.00669	0.767789	0.004474	0.75407
-0.00645	0.767517	0.004873	0.753608
-0.00621	0.76724	0.005281	0.75314
-0.00597	0.766959	0.005696	0.752666
-0.00573	0.766673	0.00612	0.752187
-0.00548	0.766382	0.006552	0.751701

0.006992	0.75121	0.039589	0.721852
0.007442	0.750713	0.040701	0.72101
0.007901	0.75021	0.041836	0.720159
0.008368	0.7497	0.042993	0.719297
0.008846	0.749184	0.044174	0.718426
0.009333	0.748662	0.045379	0.717545
0.009829	0.748134	0.046608	0.716654
0.010336	0.747599	0.047862	0.715753
0.010854	0.747058	0.049141	0.714842
0.011381	0.746511	0.050446	0.71392
0.01192	0.745957	0.051777	0.712987
0.012469	0.745396	0.053134	0.712044
0.01303	0.744828	0.05452	0.71109
0.013602	0.744254	0.055933	0.710126
0.014186	0.743673	0.057374	0.70915
0.014781	0.743085	0.058844	0.708163
0.015389	0.74249	0.060344	0.707165
0.016009	0.741888	0.061874	0.706156
0.016642	0.741279	0.063435	0.705135
0.017288	0.740663	0.065027	0.704102
0.017947	0.740039	0.066651	0.703058
0.01862	0.739408	0.068308	0.702001
0.019306	0.73877	0.069998	0.700933
0.020006	0.738124	0.071721	0.699853
0.020721	0.737471	0.07348	0.69876
0.02145	0.736809	0.075274	0.697655
0.022194	0.736141	0.077103	0.696537
0.022953	0.735464	0.07897	0.695407
0.023728	0.73478	0.080874	0.694263
0.024519	0.734087	0.082816	0.693107
0.025325	0.733387	0.084797	0.691938
0.026148	0.732678	0.086818	0.690755
0.026988	0.731961	0.088879	0.689558
0.027845	0.731236	0.090982	0.688349
0.028719	0.730502	0.093127	0.687125
0.029611	0.72976	0.095315	0.685887
0.030521	0.729009	0.097548	0.684635
0.03145	0.72825	0.099825	0.683369
0.032397	0.727482	0.102148	0.682089
0.033364	0.726705	0.104517	0.680793
0.03435	0.725919	0.106935	0.679483
0.035356	0.725124	0.109401	0.678158
0.036383	0.72432	0.111916	0.676818
0.03743	0.723507	0.114483	0.675463
0.038499	0.722684	0.117101	0.674092

0.119772	0.672705	0.318598	0.590158
0.122498	0.671302	0.32549	0.587767
0.125278	0.669884	0.332532	0.585345
0.128114	0.668448	0.339728	0.582892
0.131008	0.666997	0.347083	0.580408
0.133961	0.665528	0.3546	0.577892
0.136973	0.664043	0.362283	0.575343
0.140047	0.662541	0.370137	0.572761
0.143183	0.661021	0.378166	0.570146
0.146383	0.659484	0.386374	0.567496
0.149648	0.657929	0.394767	0.564811
0.152979	0.656355	0.403348	0.562091
0.156378	0.654764	0.412124	0.559334
0.159847	0.653154	0.421099	0.55654
0.163387	0.651525	0.430278	0.553709
0.166999	0.649877	0.439668	0.55084
0.170686	0.64821	0.449273	0.547931
0.174448	0.646524	0.4591	0.544982
0.178287	0.644818	0.469154	0.541993
0.182205	0.643091	0.479442	0.538962
0.186204	0.641345	0.489971	0.535888
0.190286	0.639578	0.500747	0.532772
0.194452	0.63779	0.511777	0.529611
0.198704	0.63598	0.523069	0.526404
0.203045	0.63415	0.53463	0.523152
0.207475	0.632297	0.546468	0.519852
0.211998	0.630423	0.558591	0.516504
0.216615	0.628526	0.571007	0.513107
0.221329	0.626607	0.583726	0.509659
0.226141	0.624664	0.596756	0.506159
0.231054	0.622698	0.610107	0.502606
0.23607	0.620709	0.623789	0.498999
0.241192	0.618695	0.637811	0.495336
0.246422	0.616657	0.652185	0.491615
0.251763	0.614595	0.666922	0.487836
0.257216	0.612507	0.682034	0.483997
0.262786	0.610394	0.697532	0.480096
0.268473	0.608254	0.713429	0.476131
0.274283	0.606089	0.729739	0.472101
0.280216	0.603897	0.746475	0.468004
0.286277	0.601677	0.763652	0.463837
0.292468	0.599431	0.781285	0.459599
0.298792	0.597156	0.799391	0.455288
0.305253	0.594852	0.817984	0.4509
0.311854	0.59252	0.837084	0.446434

0.856709	0.441888	1.437567	0.320623
0.876878	0.437258	1.476682	0.313074
0.897611	0.432541	1.517328	0.305278
0.91893	0.427734	1.559614	0.297217
0.940858	0.422835	1.603657	0.288868
0.963419	0.417839	1.649595	0.280205
0.986638	0.412743	1.697582	0.271196
1.010543	0.407543	1.747801	0.261807
1.035162	0.402234	1.800461	0.251995
1.060525	0.396812	1.855814	0.241706
1.086665	0.391273	1.914163	0.230877
1.113618	0.38561	1.97588	0.219429
1.141419	0.379818	2.041432	0.207256
1.170109	0.37389	2.111429	0.194224
1.19973	0.36782	2.186685	0.180144
1.230329	0.361601	2.26835	0.164748
1.261956	0.355224	2.358151	0.147624
1.294663	0.34868	2.458937	0.128079
1.328511	0.34196	2.576154	0.104766
1.363563	0.335052	2.723587	0.074216
1.399889	0.327944	3.04265	0